Strength in Numbers: The Tail End of Typhoon Songda Combines with Local Cyclones to Generate Extreme Sea Level Oscillations on the British Columbia and Washington Coasts during Mid-October 2016

ALEXANDER B. RABINOVICH,[a,b] JADRANKA ŠEPIĆ,[c] AND RICHARD E. THOMSON[a]

[a] *Institute of Ocean Sciences, Fisheries and Oceans Canada, Sidney, British Columbia, Canada*
[b] *Shirshov Institute of Oceanology, Russian Academy of Sciences, Moscow, Russia*
[c] *Faculty of Science, University of Split, Split, Croatia*

ABSTRACT: From 12 to 16 October 2016, a series of three major low pressure systems, including the tail end of Typhoon Songda, crossed the coasts of British Columbia (BC) and the state of Washington (WA). Songda was generated on 2 October and, after traveling northward along the coast of Japan, turned eastward toward North America. Once there, it merged with two extratropical cyclones moving along the coast of Vancouver Island. The combined lows generated pronounced storm surges, seiches, and infragravity waves off southern BC and northern WA. Here, we examine the event in terms of sea levels measured by tide gauges and offshore bottom pressure recorders, together with reanalysis data, and high-resolution air pressure and wind measurements from 182 meteorological stations. Surge heights during the event typically exceeded 80 cm, with maximum heights of over 100 cm observed at La Push (WA) and New Westminster (BC). At Tofino, on the west coast of Vancouver Island, there was a sharp 40-cm increase in sea level on 14 October in response to a marked air pressure disturbance; slightly lower sea level peaks were also observed at other outer coast locations. In all cases, the sea level response was 1.5–2.5 times as great as that expected from the inverted barometer effect, consistent with local topographic amplification. The sea level oscillations at Tofino had the form of a forced solitary wave ("meteorological tsunami," or meteotsunami), whereas those on the southwestern shelf off Vancouver Island are well described by classical standing-wave theory. A numerical model closely reproduces the observed meteotsunami peaks and standing-wave oscillations.

KEYWORDS: Extratropical cyclones; Sea level; Storm surges; Tropical cyclones; Ocean models

1. Introduction

On 2 October 2016, a low pressure trough began to develop 1600 km to the southwest of Hawaii. The system subsequently moved into the western Pacific (Fig. 1) and, on 3 October, was classified as a tropical depression by the Japan Meteorological Agency (JMA). Late on 7 October, the Joint Typhoon Warning Center (JTWC) issued a Tropical Cyclone Formation Alert for the system. The next day, the JMA upgraded the system to a tropical storm and named it *Songda* (Vietnamese: *sông Đà*, meaning "dark brown river"). On 10 October, both the JMA and JTWC reported that Songda had developed into a typhoon. Turning northward, the typhoon rapidly intensified and began to accelerate (Fig. 1a).

Typhoon Songda reintensified in the afternoon of 11 October as it moved northeastward at speed of 95 km h^{-1} (Fig. 1) and, at a latitude of ~30°N, reached its peak intensity, with 10-min maximum winds of 185 km h^{-1}, gusts of 240 km h^{-1} and a central pressure of 925 hPa. Two days later, Songda was downgraded to a severe tropical storm, moving eastward. On 15 October it turned northeastward and explosively intensified (Fig. 1b). At 1800 UTC 15 October, the Ocean Prediction Center (OPC) reported that post-tropical cyclone Songda, then 265 km west of Astoria, Oregon, had developed into a hurricane-force low with a central pressure of 969 hPa. Shortly after, Songda weakened to storm force and began tracking northward off Vancouver Island. Late on 16 October, the storm became attached to a stationary front associated with a complex low pressure system. At this point, the extratropical tail of Typhoon Songda became the last in a line of *three deep low pressure systems* affecting the western coasts of Canada and the United States during the period of 12–17 October 2016. In advance of the storms, the British Columbia, Canada (BC), cities of Victoria and Vancouver closed public parks and a number of large ferry sailings to Vancouver Island were canceled. The highest recorded wind gust during this event was 111 km h^{-1} at Race Rocks on the southern tip of Vancouver Island. At the height of the event, as many as 34 000 residents were left without power [https://en.wikipedia.org/wiki/Typhoon_Songda_(2016)].

The combined storm systems generated pronounced sea level oscillations along the outer coasts of Washington State (WA) and Vancouver Island, in Juan de Fuca Strait, and within the southern Strait of Georgia. Storm surges on the outer and inner coasts of Vancouver Island lasted for about 5 days (12–17 October) and formed three prominent maxima recorded at most tide gauge stations. The systems also generated strong seiches, marked infragravity waves, and a tsunami-like wave setup (a meteorological tsunami, or "meteotsunami"; cf. Monserrat et al. 2006). As they crossed the shelf off the western coast of Vancouver Island, the lows forced strong surface

---

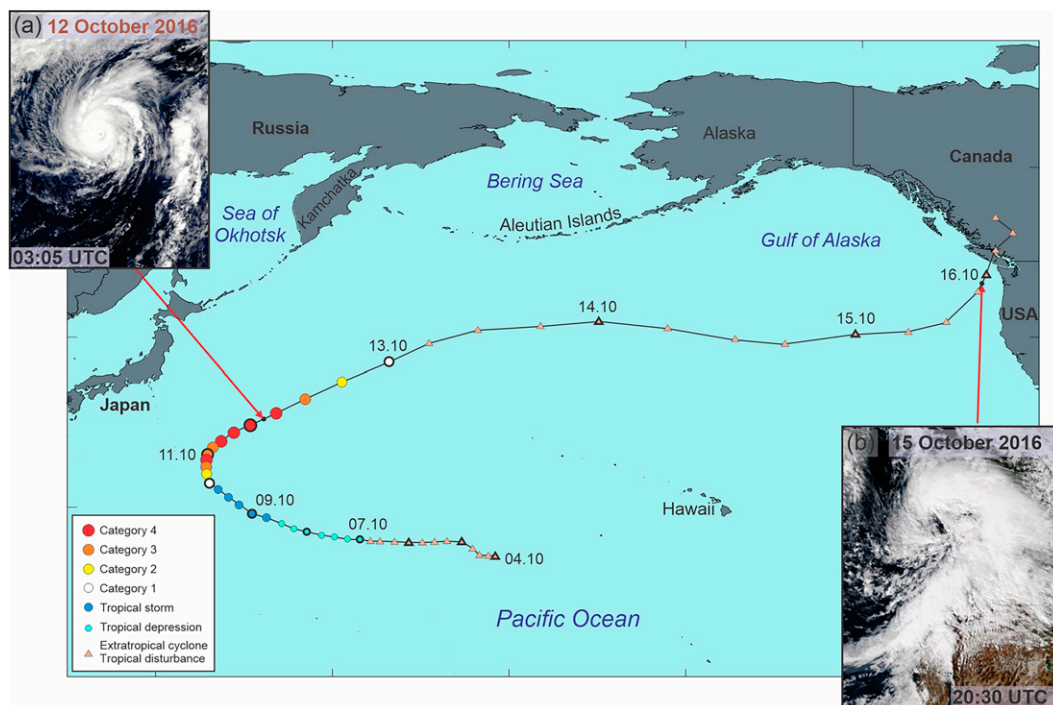*Corresponding author*: Jadranka Šepić, jadranka.sepic@pmfst.hr

FIG. 1. Track and intensity of the October 2016 Typhoon Songda according to the Saffir–Simpson scale. Tracking data are from the Joint Typhoon Warning Center. The two insets show visible images of Typhoon Songda: (a) at 0305 UTC 12 Oct 2016, captured by NASA's *Aqua* satellite (credit: NASA Goddard MODIS Rapid Response Team) and (b) Songda as a hurricane-force low near western WA at 2030 UTC 15 Oct 2016 [credit: Typhoon Songda (2016), VIIRS image captured by NOAA's *Suomi NPP* satellite, from Wikipedia].

ocean currents with speeds of >50 cm s^{-1}, as recorded on 14 October by the high-frequency (HF) WERA radar system installed by Ocean Networks Canada (ONC) near Tofino; the system issued an automatic alert about anomalously strong currents in the region (Dzvonkovskaya 2018).

The forcing of barotropic waves by moving storms has been investigated by a number of authors. Mercer et al. (2002) examined strong tsunami-like oscillations on the east coast of Newfoundland caused by Tropical Storm Helene traveling across the Grand Banks. Similarly, Vennell (2007) studied the generation of transient ocean waves by small fast-moving storms affecting the east coast of New Zealand. Using one- and two-dimensional numerical models, the author showed that amplified waves are mostly formed by air pressure disturbances propagating across the shallow-water continental shelf. Williams et al. (2019) described and numerically simulated intense meteotsunamis in the English Channel generated by a heavily precipitating convective storm moving northeastward with a speed of ~19 m s^{-1}. Recently, Heidarzadeh and Rabinovich (2021) examined extreme sea level variations produced by Typhoons Lionrock (2016) and Jebi (2018) that destructively impacted the coast of Japan. According to these studies, the multiple deaths and extensive floods on the Japanese coast were due to the combined effect of a low-frequency sea level rise caused by storm surges and intense high-frequency waves associated with a meteotsunami. Similar cumulative destructive effects associated with a storm surge, extreme seiches, and

infragravity waves generated by Typhoon Maysak passing over the Sea of Japan were investigated by Medvedev et al. (2022).

The present study has a threefold purpose: 1) to examine the series of atmospherically induced sea level oscillations affecting the coasts of southern BC and WA during 12–17 October 2016, 2) to estimate the fundamental properties of these oscillations, and 3) to numerically model the physical mechanism responsible for formation of the extreme sea levels. The two main noteworthy aspects of this event are well-defined sea level responses at each observational site and a unique set of precise sea level, bottom pressure, and air pressure data enabling us to characterize the "Songda event" with much higher spatial and temporal resolution than is typically possible.

2. Observations

The storm surges and tsunami-like waves associated with the Songda event were recorded by a large number of permanent and temporary Canadian Hydrographic Service (CHS; https://www.tides.gc.ca/tides/en/stations) tide gauges along the coast of BC (Fig. 2). All tide gauges were precise high-resolution digital instruments (cf. Rabinovich and Stephenson 2004) with a 1-min sampling interval. Similar U.S. National Oceanic and Atmospheric Administration (NOAA; https://tidesandcurrents.noaa.gov/) gauges recorded strong sea level oscillations associated
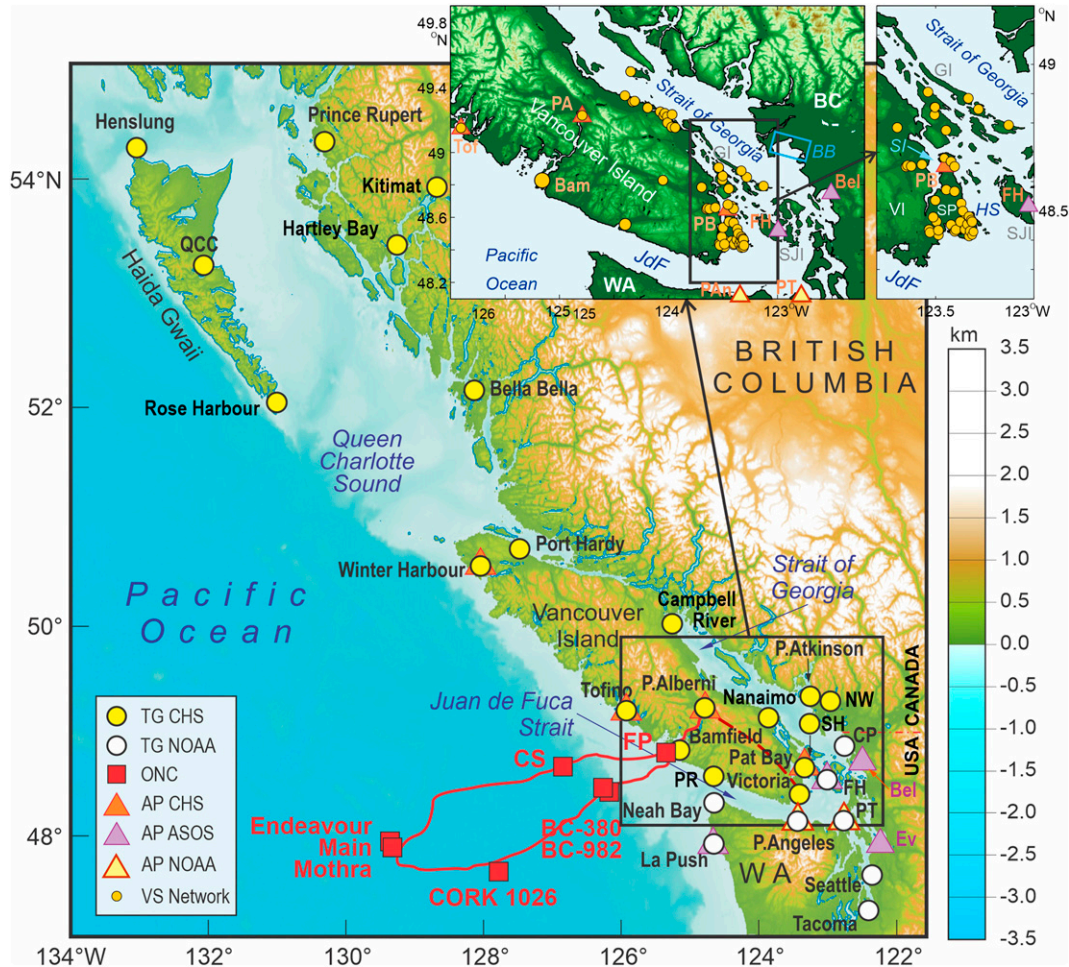
FIG. 2. Map of coastal BC and northern WA showing locations of the CHS and NOAA coastal tide gauges (TG). Also shown are the locations of 7 ONC NEPTUNE BPRs offshore of southwestern Vancouver Island and 11 microbarographs (label AP): 4 CHS (Tofino, Winter Harbor, Patricia Bay, and Port Alberni), 3 NOAA (Port Angeles, Port Townsend, and Friday Harbor), and 4 U.S. ASOS sites (Bellingham, Everett, Friday Harbor, and La Push). The insets show the Victoria School ("VS") network of meteorological stations indicated by small yellow circles. The enlarged circle "Bam" denotes the Bamfield VS station used for the frequency time analysis together with the CHS microbarographs. Abbreviations are as follows: 1) ONC BPRs: BC = Barkley Canyon (380- and 982-m depths), CS = Clayoquot Slope, FP = Folger Passage; 2) CHS: QCC = Queen Charlotte City, NW = New Westminster, SH = Sand Heads, PR = Port Renfrew, 3) NOAA: FH = Friday Harbor, CP = Cherry Point, PT = Port Townsend; and 4) AP: Tof = Tofino, PA = Port Alberni, PB = Patricia Bay, PAn = Port Angeles, Ev = Everett, Bel = Bellingham. Other abbreviations are as follows: JdF = Juan de Fuca Strait, HS = Haro Strait, SI = Saanich Inlet, BB = Boundary Bay, VI = Vancouver Island, SP = the Saanich Peninsula, SJI = the San Juan Islands, and GI = the Gulf Islands.

with this event on the coast of WA. Here, we have used sea level time series from tide gauges located in the northern part of WA, including those on the coasts of Juan de Fuca Strait, Puget Sound, and the southern Strait of Georgia (Fig. 2).

This event was also recorded off southwestern Vancouver Island by bottom pressure recorders (BPRs) within the NEPTUNE-Canada cabled observatory array of ONC (version 2.0). An important component of the network is the real-time measurement of tsunami waves as they cross the flat abyssal plain region of Cascadia Basin and propagate over the continental slope and shelf (cf. Thomson et al. 2011). In this study, we

have used seven BPRs: 1) Endeavour Main (depth 2195 m), located at the westernmost flank of a 825-km bottom cable loop; 2) Endeavour Mothra (2275 m), located 3.5 km south of Endeavour Main; 3) Ocean Drilling Program (ODP) CORK 1026 observatory (2654 m) located in Cascadia Basin on the southern side of the cable loop; 4) Clayoquot Slope (1200 m) at the northern flank of the loop; 5) Barkley Canyon 982 (982 m) located on the canyon axis; 6) Barkley Canyon 380 (380 m) on the northern slope of the canyon; and 7) Folger Passage (96 m), located at the mouth of Barkley Sound, offshore of Vancouver Island near Bamfield (Fig. 2). The 1-s, ~0.1-mm vertical resolution sea level oscillations provided by

these instruments were low-pass filtered with a 2-min Kaiser–Bessel (KB) window and then resampled at 1 min.

On the atmospheric side, we have used a unique set of high-resolution 1-min sampled air pressure and wind records from the Victoria School-Based Weather Station Network (herein, the "VS network") of 171 meteorological stations located mainly in the southern part of Vancouver Island and on the Gulf Islands (see insets in Fig. 2) (www.victoriaweather.ca; Weaver and Wiebe 2006). Additional atmospheric observations are provided at 1-min sampling by four CHS stations (Patricia Bay, Port Alberni, Tofino, and Winter Harbour), combined with the corresponding permanent tide gauges, and by four U.S. Automated Surface Observing System (ASOS; https://mesonet.agron.iastate.edu/) weather stations (Bellingham, Friday Harbor, Everett, and La Push) and three NOAA stations (Port Angeles, Friday Harbor, and Port Townsend) with 6-min sampling at corresponding tide gauge sites (Fig. 2). Altogether, we used meteorological data from 182 weather stations, which has enabled us to examine both the spatial and temporal structure of mesoscale atmospheric disturbances during the Songda event and to estimate the general characteristics of atmospheric processes in this region, in particular, precise estimation of the disturbance speeds, directions, and frequency dispersion based on the procedure described by Rabinovich et al. (2021).

In addition to the tide gauge records, offshore BPR data, and VS network meteorological data, we used synoptic, near-surface atmospheric wind and pressure fields, plus high-altitude weather and wind maps, to characterize air–sea conditions at the time of the Songda event. The latter were obtained from ERA5 (fifth-generation records of the ECMWF atmospheric reanalyses of the global climate; Hersbach et al. 2020), accessed through the Copernicus Climate Data Store (CDS).

3. Analysis of meteorological processes

a. Synoptic-scale motions

Our analysis of the ERA5 hourly mean sea level pressure (MSLP) and 10-m winds reveals that, during the course of three days (14–17 October), three separate MSLP lows passed over Vancouver Island (Fig. 3). The first low pressure system to reach the island (L1) developed west of WA in the early morning of 14 October (Figs. 3b,c, purple). From there, it propagated northeastward, coming close to the northwestern coast of Vancouver Island within 6 h. The center of L1 did not cross the island, but rather grazed it, with its eastern flank coming within half the distance between Tofino and Winter Harbour. Based on the ERA5 reanalysis data, the low was deepest (972.6 hPa) offshore of Tofino, which was also the region attaining the strongest onshore winds (speeds > 15 m s^{-1}).

The second low (L2) developed farther offshore (Figs. 3a–d, green) during the afternoon of 13 October 2016. The low reached its maximum depth (968.7 hPa) close to the generation area, from where it propagated east-northeastward toward Vancouver Island, crossing the coast over Barkley Sound and Alberni Inlet. By the time it reached Vancouver Island, L2 had already weakened (977.2 hPa) (Fig. 3d). The highest

winds (up to 24 m s^{-1}) appeared over the open sea, along the low's southern flank. The strongest coastal onshore winds, up to 20 m s^{-1}, hit the western coast of WA (Fig. 3d). Over Vancouver Island, the most intense winds (up to 15 m s^{-1}) were seaward of the Tofino-Barkley Sound region.

The third low pressure system (L3) was the tail end of Typhoon Songda (Figs. 3d–f, orange). As noted earlier, Songda reintensified off the coast of Oregon (attaining a MSLP depth of 972.8 hPa) and had weakened slightly to 976.6 hPa by the time it hit Vancouver Island. The strongest winds (>22 m s^{-1}) impacted the coasts of Oregon and WA. L3 had almost the same pathway over Vancouver Island as L2, passing over Barkley Sound and Alberni Inlet (Fig. 3d), with similar wind speeds of up to 15 m s^{-1}.

The occurrences of the three distinct lows (L1–L3) in the ERA5 data are clearly evident in the air pressure and wind records for selected CHS, NOAA, and VS network sites (Fig. 4). Further analysis of the observations reveals that there was yet another pressure minimum (L4) over the Saanich Peninsula and northern WA that was not resolved in the ERA5 data. It is difficult to distinguish L3 from L4 in the time series (Fig. 4), as L3 seems to be embedded within L4. However, our analysis of the arrival times of air pressure extrema at the various stations reveals two individual minima propagating at different speeds and directions (cf. Fig. 3c). Wind speeds significantly increased during the passage of wind gusts accompanying the MSLP lows crossing over the island, reaching values higher than 6 m s^{-1} at most stations. The time series further indicate considerable spatial variability in the wind distribution over Vancouver Island. In the northwestern part of the island (Stations 179 and 180), there were three periods with pronounced wind activity, all coinciding with the passage of MSLP lows. The strongest winds (speeds up to 11 m s^{-1}, gusts up to 22 m s^{-1}) were associated with L1 as it propagated over this area (Fig. 3). In the central part of the island (stations 196 to 226), the periods of amplified wind were the longest (because this was the area affected by all three lows and over which L2 and L3 were deepest). Over the Saanich Peninsula (see the right inset in Fig. 2 for the peninsula location), the periods of intensified wind were relatively short (maximum 12 h) and associated with the passage of L2, L3, and L4. Nevertheless, the winds recorded there had strengths comparable to or even stronger (up to ~25 m s^{-1}) than those in the central part of the island.

b. High-frequency air pressure disturbances

A detailed examination of the air pressure time series reveals that there were distinct high-frequency (HF) air pressure disturbances embedded within each of the three MSLP lows. The most energetic air pressure disturbance (AD1) was linked to system L1 (Fig. 5). Rates of air pressure changes within AD1 reached 2.8 hPa (10 min)$^{-1}$ and heights up to 6.0 hPa, with the maximum at Station 992 (Tofino) (Fig. 6). The strength of AD1 was comparable to that at Tofino for other stations within Barkley Sound (Station 161) and Alberni Inlet (Stations 165, 166, and 993), but AD1 weakened quickly as it propagated northwestward over Vancouver Island.
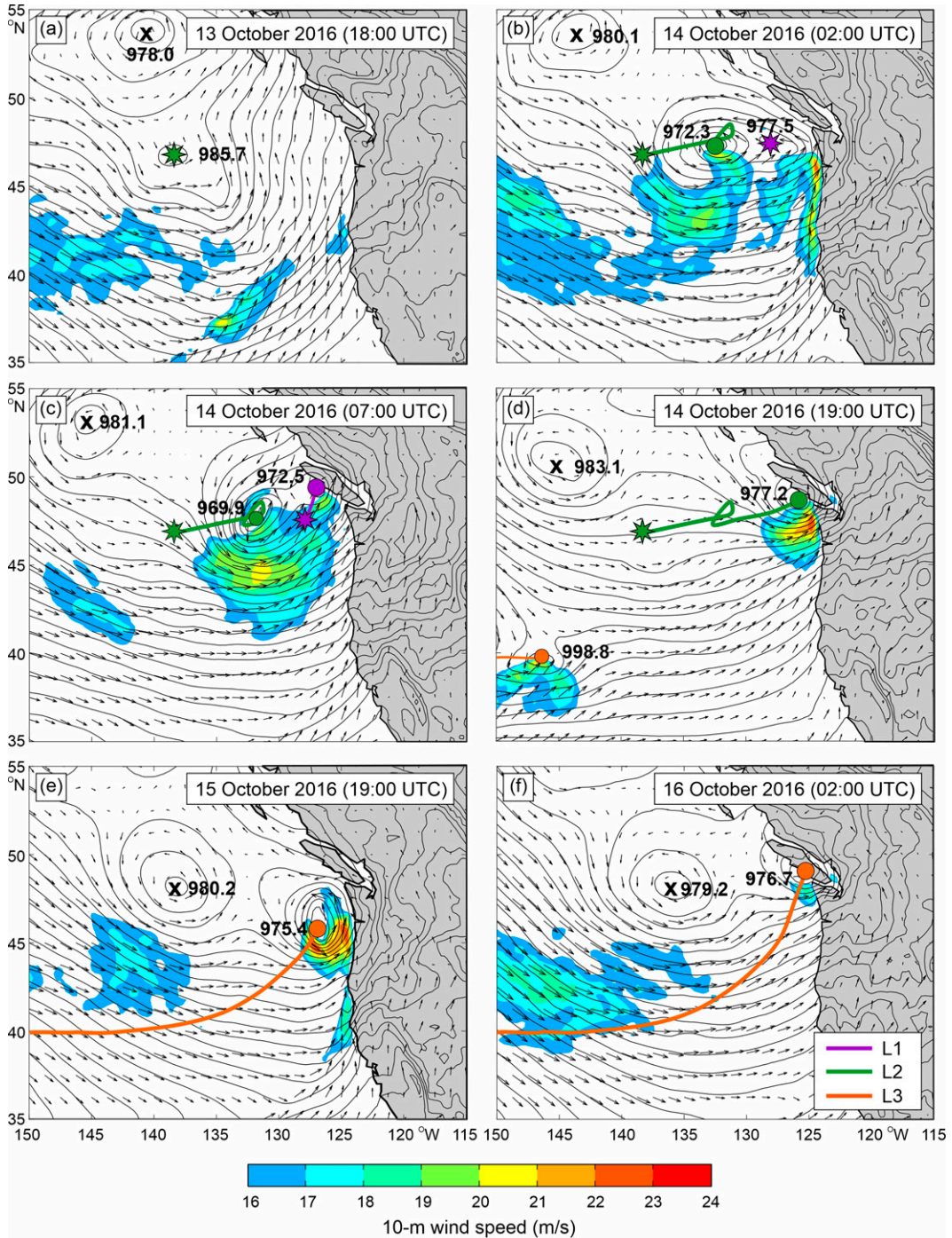
FIG. 3. The ERA5 MSLP and 10-m wind velocity fields in 2016, at (a) 1800 UTC 13 Oct, (b) 0200 UTC 14 Oct, (c) 0700 UTC 14 Oct, (d) 1900 UTC 14 Oct, (e) 1900 UTC 15 Oct, and (f) 0200 UTC 16 Oct 2016. Three air pressure lows are depicted with various colors; L1 with purple, L2 with green, and L3 with orange. Lines show their trajectory, stars show their generation point, and circles show their location at a given time. The MSLP minimum related to the Aleutian low is indicated by an X. Values of minimum pressure (hPa) related to lows are given. Isobars are shown with a 2-hPa step. Only wind speeds higher than 16 m s^{-1} are colored.
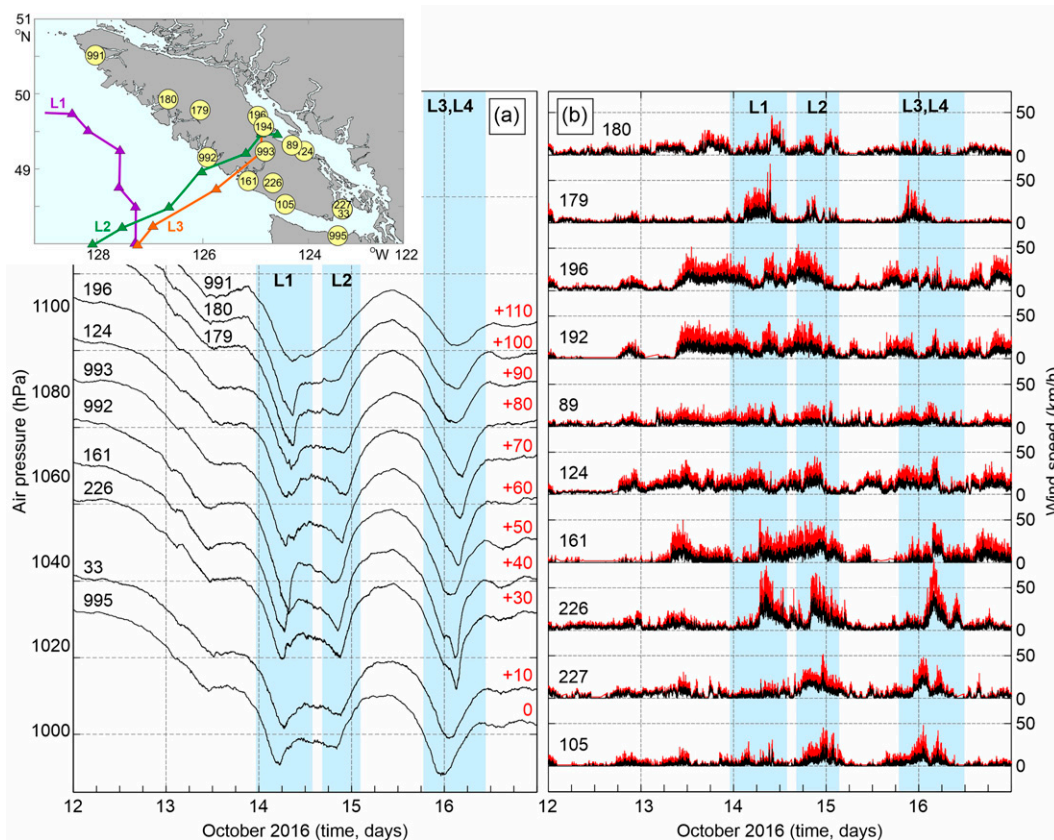
FIG. 4. (a) Air pressure and (b) wind speed (black) and wind gust (red) time series measured at selected VS network, CHS (991, 992, and 993), and NOAA (995) stations. Station locations and trajectories of low pressure events L1–L3 are given in the inset. Light-blue bands indicate periods of the MSLP minima presence over the network.

The HF air pressure disturbance (AD2) associated with system L2 was the weakest of the three disturbances, with maximum rates of air pressure change less than 1.2 hPa $(10 \text{ min})^{-1}$ and maximum air pressure oscillations of 3.0 hPa (Fig. 5). Maximum values were recorded along the eastern side of Barkley Sound (Station 161) and within Alberni Inlet (Stations 165, 166, and 993), coinciding with the path of L2 (Fig. 6).

High-frequency disturbance AD3, associated with low L3 was, like AD1, very energetic, reaching maximum rates of air pressure change of up to 2.0 hPa $(10 \text{ min})^{-1}$ and maximum heights of 5.0 hPa at stations 161 and 226 (Fig. 5). Maximum values were again recorded along the eastern side of Barkley Sound (Fig. 6).

c. Properties of the atmospheric disturbances

For numerical modeling purposes, we need to know the trajectories and parameters of the atmospheric disturbances that crossed Vancouver Island (Figs. 3 and 4). Following Thomson et al. (2009) and Rabinovich et al. (2021), we used the least squares method to estimate velocity vectors of the four MSLP lows (L1–L4) (Fig. 6a; Table 1) and three high-frequency atmospheric disturbances (AD1–AD3) (Fig. 6b; Table 2). According to the estimates in Table 1, L1 propagated to the north-northeast with a mean speed of 14.2 m s^{-1}. The high

precision velocity estimates (Table 1, Fig. 6a) demonstrated that the eastern section of L1 moved slower than the western section, resulting in the low's spatial deformation. Similarly, L1 was deeper along the outer coast of the island (minima from 968 to 976 hPa) than along the inner coast (976–984 hPa).

The HF air pressure disturbance, AD1, that accompanied L1 propagated with a different speed and direction than the parent disturbance, with AD1 propagating much faster (21.1 m s^{-1}) and toward the northwest (Table 2). At stations along the outer coast of Vancouver Island, the time offset between peak values of L1 and AD1 was only ~20 min, indicating that they affected this coast almost simultaneously, whereas along the inner coast the time difference increased up to ~60 min. Of the three main lows that transited Vancouver Island, L3 was the deepest. Along its center line, L3 reached minimum depths of 968–972 hPa, weakening toward its outskirts to 972–980 hPa. The high-frequency disturbance AD3 embedded in L3 moved toward the north-northeast with a speed of 19 m s^{-1} (Table 2). The low with the smallest extent, L4, was characterized by minimum air pressure values of 972–980 hPa and propagated to the north-northeast at a speed of 19.2 m s^{-1}, crossing Vancouver Island in ~40 min.

The high spatial and temporal resolution of the VS network weather stations provided us with a unique opportunity to estimate not only the propagation velocities of the high-frequency
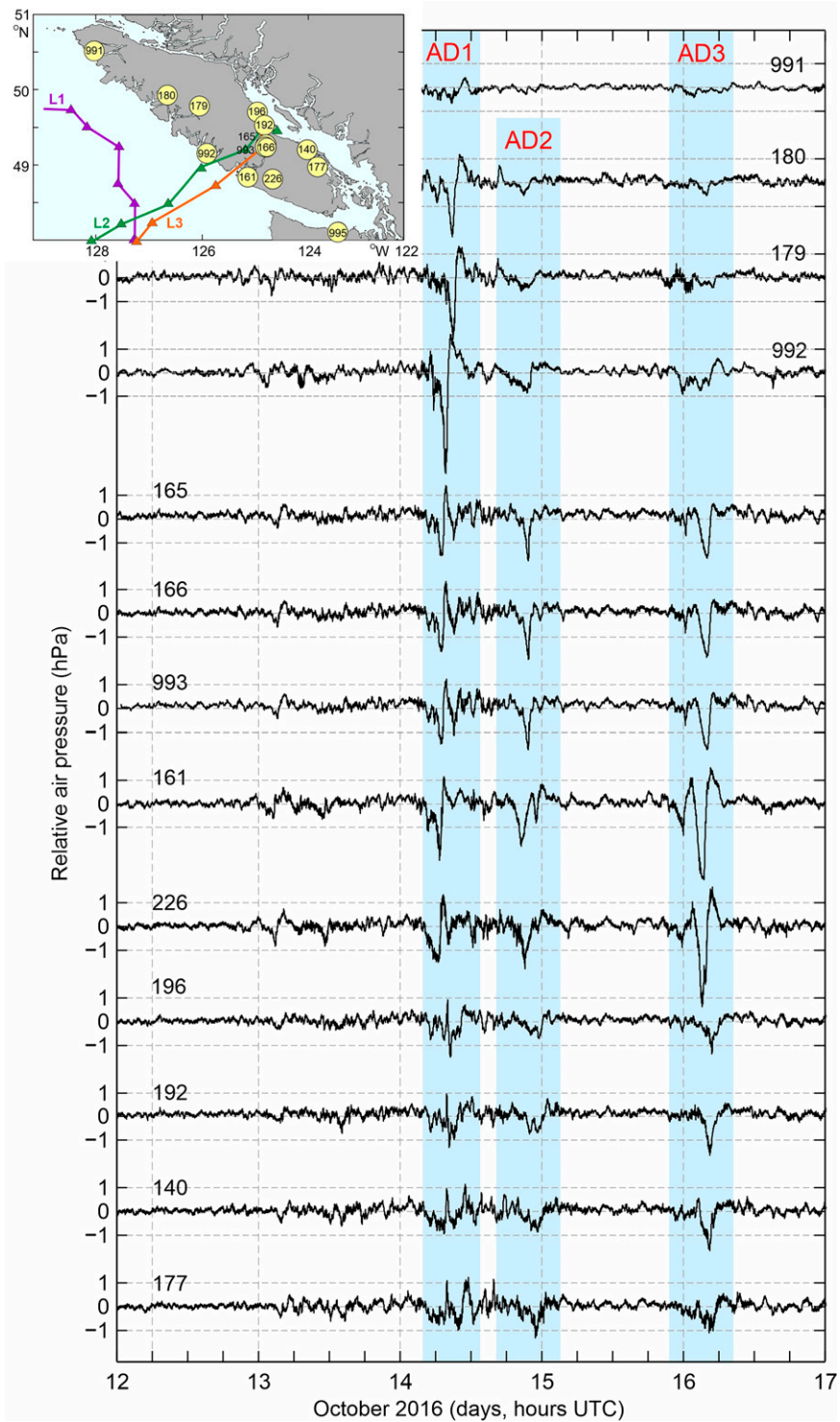
FIG. 5. High-pass (with a 4-h KB window) air pressure time series measured at selected VS network, CHS, and NOAA sites. Light-blue bands indicate disturbances AD1–AD3. Station locations and trajectories of L1–L3 are given in the inset.
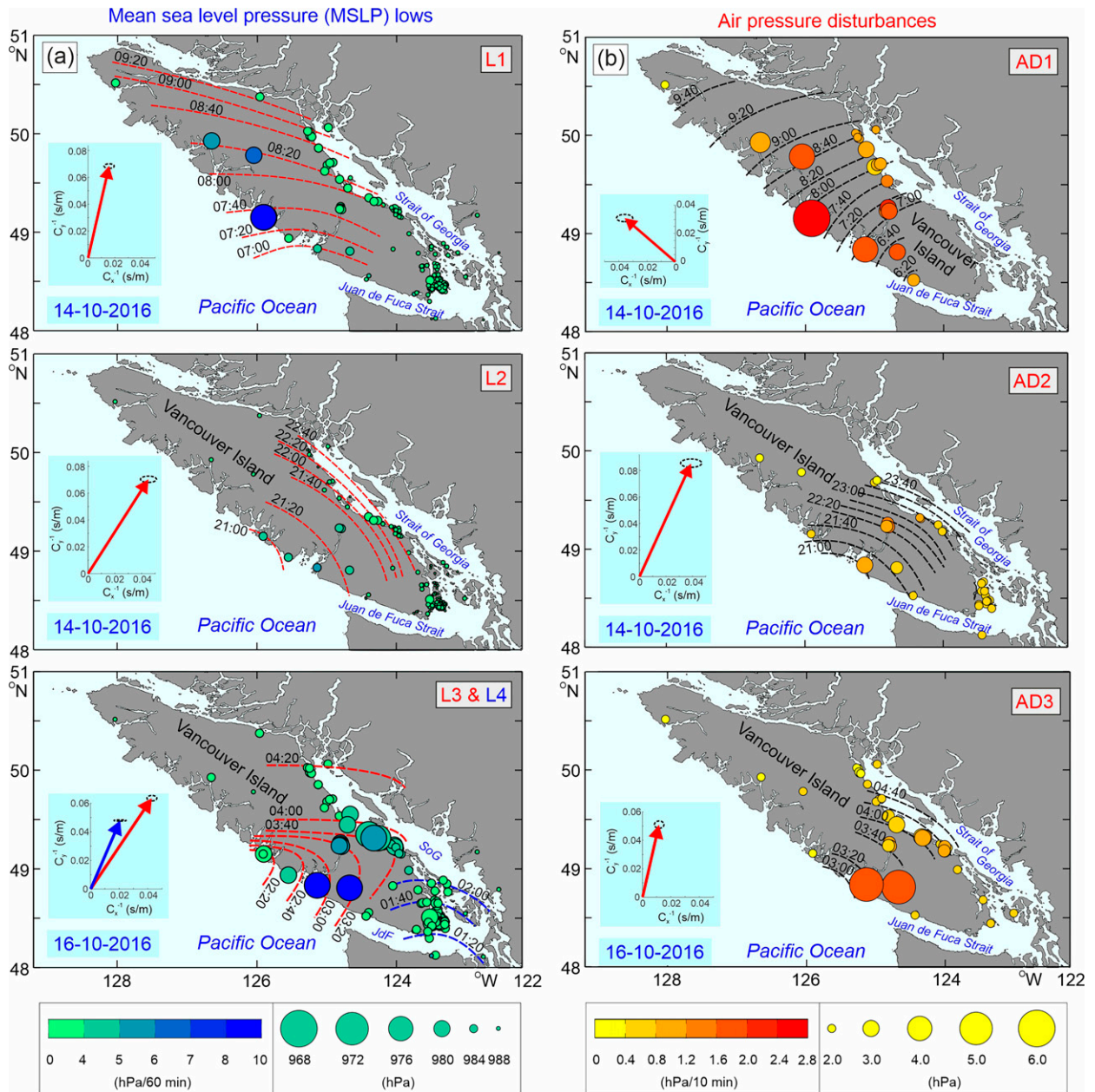
FIG. 6. Isochrones of the arrival times of air pressure disturbances crossing Vancouver Island during 14–16 Oct 2016: (a) the four distinct MSLP minima and (b) the three high-frequency disturbances. The inverse velocity vectors (s m^{-1}) for the propagating disturbances in (a) and (b) are plotted in the insets, together with their 95% error ellipses.

atmospheric disturbances, but also their cross-track characteristics. According to our analysis, air pressure disturbances AD1–AD3 were strongest along central propagation lines and diminished in the cross-propagation direction (Figs. 5 and 6d). Herein, the central line defines the disturbance's velocity vector and passes through the reference station chosen as the station recording the strongest disturbance. To approximate the cross-track disturbance structure and thus estimate a more precise rate of cross-track attenuation, we experimented with three types of functions (Gaussian, exponential, and bell-shaped)

and found that the best fit is achieved with the bell-shaped function (Fig. 7),

$$f(x) = \frac{a}{1 + \left| \dfrac{x - b}{c} \right|^{2d}}, \tag{1}$$

where x is the cross-track distance from the reference station, a is the disturbance amplitude, b is the position of the disturbance maximum relative to the reference station, c is the half-width, and d is a slope parameter (Table 2).

TABLE 1. Propagation speed U, direction θ (°true), and respective errors (ε_U and ε_θ) for the four MSLP lows propagating over Vancouver Island in mid-October 2016. The second column gives the number of measurement sites used in the analysis.

MSLP low	No. of stations	U (m s^{-1})	ε_U (m s^{-1})	θ (°)	ε_θ (°)
L1	22	14.2	±1.2	192.9	±3.9
L2	28	11.9	±1.7	212.7	±2.9
L3	22	13.1	±1.1	214.0	±2.8
L4	52	19.2	±3.1	203.4	±1.0

The bell-shaped function closely approximates the two stronger atmospheric disturbances AD1 and AD3 (Fig. 7) for which both visual and statistical (high correlation coefficient squared R^2) agreements are exceptionally good. Unfortunately, our estimates for AD1 are somewhat constrained by the fact that all measuring stations are located to the right of the AD1 center, whereas to the left (i.e., over the ocean, the region of specific interest) there are no stations. The half-width [parameter c; Eq. (1), Table 2] for AD1 and AD3 was ~60–70 km, whereas for AD2 it was significantly larger (93.5 km).

4. Coastal sea level oscillations

The tail end of Typhoon Songda and two associated lows produced several types of hazardous waves and extreme sea level oscillations on the outer (oceanic) coast of Vancouver Island and on other coastal regions of southern British Columbia and northern WA. As emphasized by Heidarzadeh and Rabinovich (2021) and Medvedev et al. (2022), the cumulative effect of several types of sea level oscillations superimposed on each other is one of the main reasons for the destructive consequences of typhoons and hurricanes impacting the coast. The main types of oscillations for coastal Vancouver Island include the following:

1) storm surge formed by the combined effect of low air pressure and onshore wind,
2) infragravity waves, with periods of 30–300 s, generated by the nonlinear interaction of storm waves, and
3) seiches and meteotsunamis.

a. Storm surge

As the remnant of Typhoon Songda approached the coast of British Columbia and combined with the two other lows (Figs. 1 and 3), it generated a considerable rise in sea level. Sea level rises, which were observed along both the outer (oceanic) coasts of British Columbia/WA (Fig. 8a) and on the inner coasts (Fig. 8b), lasted for about five days (12–17 October 2016) and at most stations had three prominent maxima (SL1, SL2, and SL3), with peak times of ~0600 UTC 14 October, ~1900 UTC 14 October, and ~0200 16 October 2016 ("weakened Typhoon Songda"). At Tofino, SL1 was predominant, whereas at La Push SL2 was the strongest. SL3 prevailed at most of the other stations, including those along the southwestern coast of Vancouver Island (Port Alberni, Bamfield, Port Renfrew, Victoria, and Patricia Bay) and the northern coast of WA (Neah Bay, Port Angeles, and Port Townsend) (Figs. 8a and 9). At most stations located in the Strait of Georgia, SL2 and SL3 were the strongest and had approximately the same heights (Figs. 8b and 9). Along the WA coast, sea level rise was most prominent at La Push, where SL3 reached 76 cm (117 cm from the undisturbed sea level observed before the Songda event), and along the British Columbia coast at New Westminster where SL2 reached 42 cm (93 cm from the undisturbed sea level observed before the event).

At most stations, sea level peaks were predominantly due to the storm surge component (Fig. 9), i.e., to sea level rise manifested in the low-passed (LP) (4-h KB window) series. The highest storm surges were observed in the southern part of British Columbia, including the southwestern coast of Vancouver Island, Juan de Fuca Strait, and the southern Strait of Georgia and on the oceanic coast of northern WA (Figs. 8 and 9), coinciding with the three sea level maxima (SL1, SL2, SL3). At most stations in this region, the surge heights were greater than 40 cm relative to the mean sea level (70 cm from the undisturbed sea level observed before the Songda event). Similarly, maximum storm surge, as represented by the LP values on the WA coast reached a height of 58 cm (98 cm from the undisturbed sea level observed before the Songda event) at La Push and, on the British Columbia coast, 39 cm (93 cm from the undisturbed sea level observed before the Songda event) at New Westminster located within the Fraser River. Storm surge heights rapidly diminished northward of these sites, falling to ~20 cm in northern BC. In addition to the surge component, significant high-frequency sea level oscillations were recorded at several stations, in particular, at the outer coasts of British Columbia and WA (Figs. 8a and 9). High-frequency components contributed most to the total flood height at Tofino and Port Alberni (during L1–AD1; Fig. 9a) and in La Push (during L2–AD2; Fig. 9b). Along the outer coast, northward of Tofino, the high-frequency component, was negligible, as it was in most of the inner coast stations (Fig. 9), except for Campbell River (CR) (Figs. 9b,c) and Nanaimo (Fig. 9b).

TABLE 2. Propagation speed, direction (°true), respective errors, and cross-track parameters of the high-frequency atmospheric disturbances AD1, AD2, and AD3 propagating over Vancouver Island. The cross-track parameters are defined in Eq. (1). The second column gives the number of measurement sites used in the analysis.

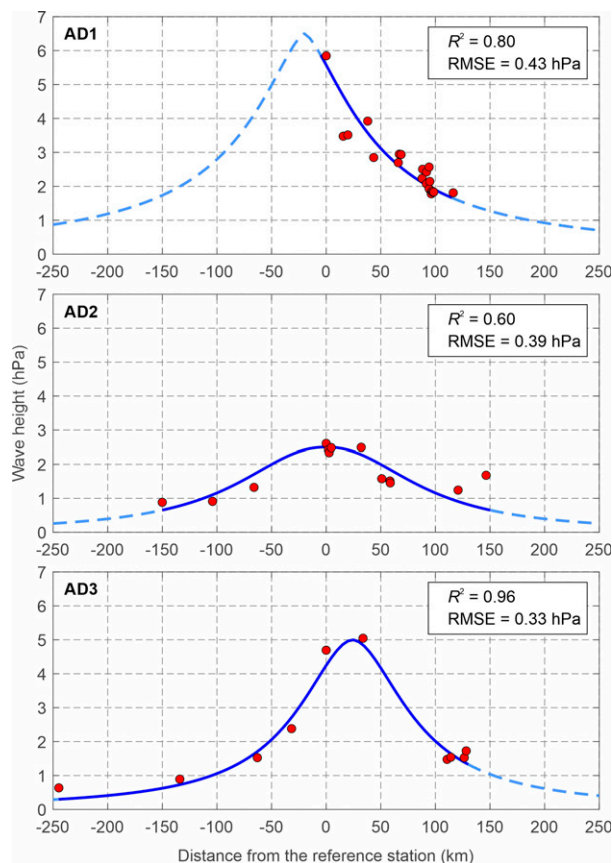| HF disturbance	No. of stations	Propagation velocity				Cross-track parameters			
		U (m s^{-1})	ε_U (m s^{-1})	θ (°)	ε_θ (°)	a (hPa)	b (km)	c (km)	D
AD1	9	21.1	±2.6	130.7	±13.9	6.5	20.0	66.3	0.75
AD2	9	10.7	±1.7	204.6	±5.3	2.5	0.0	93.5	1.10
AD3	9	19.1	±2.1	193.0	±7.2	5.0	24.2	61.3	0.95

FIG. 7. Dependence of the air pressure disturbance amplitudes on the cross-propagation distance from the reference stations Tofino (station 992, for AD1) and Bamfield (station 161, for AD2 and AD3) (see Figs. 2 and 5 for locations). Dots denote measured air pressure heights, and the blue lines are the fitted functions; a full blue line is used for fits within the station coordinates, and the dashed light-blue line is used for fits that are not covered by station coordinates. The R^2 is the square of the correlation coefficient, and RMSE is the root-mean-square error of the functional fits.

b. Sea level–air pressure relationships on the outer coast

Next, we examined in detail the sea level response to air pressure forcing at the outer coast of Vancouver Island. We have focused on this area because several of the most noteworthy processes were observed here. There are five CHS tide gauges on this coast (Fig. 2): Port Renfrew, Bamfield, Port Alberni, Tofino, and Winter Harbour. The maximum sea level heights presented in Fig. 10a are measured relative to the residual sea level at the start of the storm surges—the point where shading under the residual sea level curves begins (at approximately 0700 UTC 12 October). The common feature of all five records was a chain of individual sea level maxima superimposed on a general sea level rise. The rising sea level at these sites lasted for almost five days. During this time, the records consisted of a superposition of low-frequency sea level variations associated with storm surge (more precisely, with the sequence of three storm surges) and high-frequency oscillations due to local storm-generated seiches and infragravity (IG) waves.

To better understand the origin of the observed sea level extrema and the general character of sea level oscillations on the Pacific coast of Vancouver Island and their interaction with the atmospheric oscillations, we examined data from the four CHS air pressure records available at Patricia Bay, Port Alberni, Tofino, and Winter Harbour (Fig. 10b). There is an evident negative correlation between sea level and atmospheric pressure: the rise of sea level corresponds to the fall of air pressure and vice versa, with the three maxima of sea level (SL1, SL2, and SL3) precisely coinciding with the minima of atmospheric pressure [i.e., with three lows (L1–L3)]. The precise SL and AP values during SL1, SL2, and SL3, and the corresponding times, are given in Table 3 (for completeness, we added one more AP station: the VS network weather station at Bamfield; see the inset in Fig. 2). The three SL maxima at Tofino occurred at 0701 UTC 14 October, 1907 UTC 14 October, and 0140 UTC 16 October. At Tofino, SL1 was the largest event, whereas at the other four Vancouver Island stations SL3 was the most prominent (Fig. 10a). For the timing, at Tofino the three atmospheric pressure minima preceded the sea level maxima by 21–61 min. At Port Alberni, for SL1, the AP minimum preceded the sea level maximum by 37 min. For SL2 and SL3, the AP minima occurred after the times of the sea level maxima by 93 and 43 min, respectively. This suggests that these two surges were probably generated on the coastal shelf or in Barkley Sound and propagated from there to the head of Alberni Inlet ahead of L2 and L3 MSLP.

The general tendency for events SL1–SL3 is their intensification in the southern part of the study region and their attenuation northward. In particular, the extreme sea level heights at Winter Harbour for SL1–SL3 were smaller by a factor of approximately 2–2.5 than at Tofino, Bamfield, Port Alberni, and Port Renfrew (Table 3). Event SL2 was not detectable at Winter Harbour but was clearly present at stations to the south (Fig. 10a).

c. High-frequency oscillations

In addition to low-frequency variability, the five stations show intensification of high-frequency sea level oscillations during the passage of atmospheric disturbances AD1–AD3 (Figs. 8, 9, and 12). While the low-frequency changes at all five stations look similar, the HF oscillations of the records were significantly different. A remarkable feature of these records is the very sharp "knife-like" increase in sea level at Tofino, with a height of 52.6 cm (or 89.2 cm relative to undisturbed sea level before the event) at the time of the SL1 event. This meteotsunami is presented as Event No. 38 in the list of 1992–2019 meteotsunamis described by Rabinovich (2020). Sharp sea level peaks were also observed at Bamfield, Port Alberni, and Port Renfrew at the time of SL1, with sea level reaching maximum heights of 37.6, 42.6, and 34.9 cm, respectively. The sharp knife-like peaks in sea level recorded at Tofino, Bamfield, and Port Alberni are clearly linked to air pressure variations at these sites (Fig. 11). However, the sea level responses at these stations are roughly 11 times as great as expected from the inverse barometer effect for air pressure
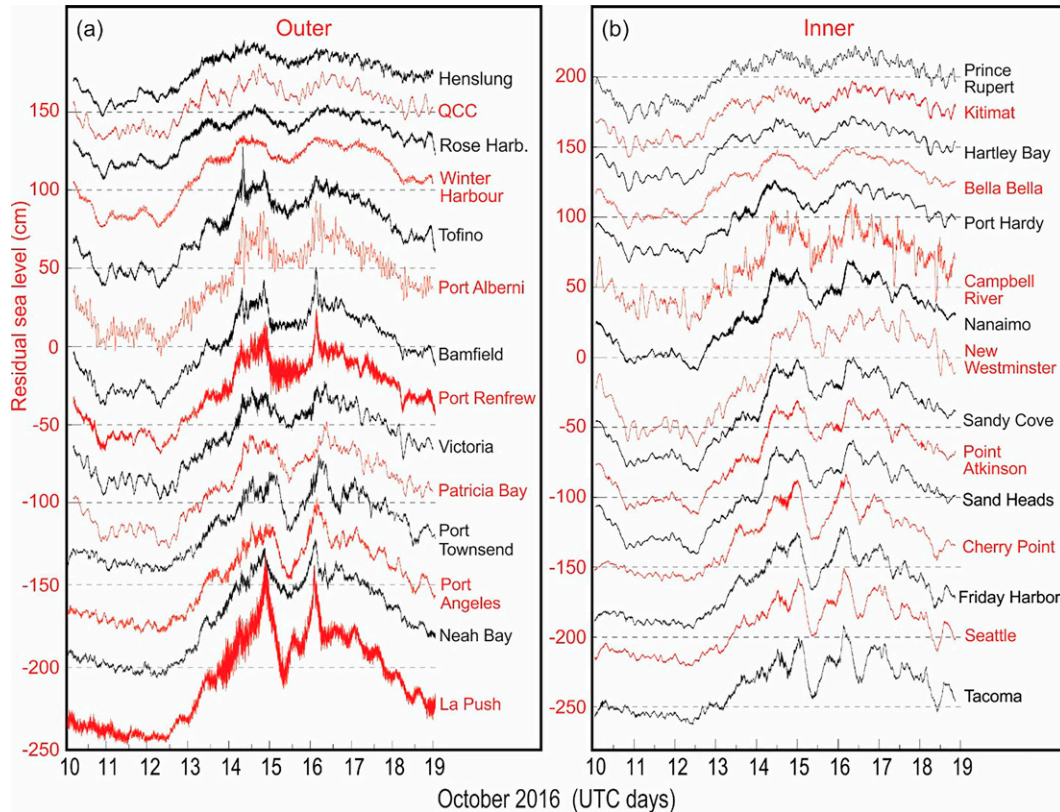
FIG. 8. The residual (detided) sea level records for the (a) outer and (b) inner coasts of BC and WA associated with the storm surges of 12–17 Oct 2016. The "inner" station Patricia Bay is shown together with the "outer" stations because it is located close to Victoria and results look similar.

disturbances, which at Tofino was only ~4.8 hPa. From this, we conclude that the sea level responses to the propagating AP disturbance were amplified by the topography and possibly by the onshore winds.

A feature specific to the Port Renfrew record was the presence of marked high-frequency oscillations, likely related to IG waves generated through the nonlinear interaction of wind waves or swell (cf. Rabinovich 2009). Such waves are predominant on open oceanic coasts and their occurrence is normally enhanced during major storms. In contrast to other stations examined in this study, Port Renfrew is exposed to incoming storm waves and therefore susceptible to IG events.

To examine temporal variations in the high-frequency sea level and air pressure oscillations in the frequency domain, we used a multiple-filter method (cf. Thomson and Emery 2014). The method is based on narrow-band filters with a Gaussian window that isolates a specific central frequency, $\omega_n = 2\pi f_n$, where f_n is the frequency, and has been effectively used to investigate various meteotsunami events (cf. Šepić and Rabinovich 2014; Heidarzadeh et al. 2020; Heidarzadeh and Rabinovich 2021; Rabinovich et al. 2021). The method enables us to examine the nonstationary character of the propagating waves as a function of frequency f and time t. The "f–t diagrams" for the frequency band of 0.2–30 cph (periods from 5 h to 2 min) for five tide gauge and air pressure records for the 4-day

segments of 13–16 October 2016 are presented in Figs. 12a and 12b, respectively.

Distinct features of the f–t sea level diagrams are the well-defined, relatively narrow frequency bands of amplified energy. The stability and the persistent character of these oscillations throughout 14–16 October support the notion that the oscillations were tuned to the eigen (resonant) periods of the sites:

- 4–5, 30, and 50 min for Winter Harbour;
- 20, 48, and 100 min for Tofino;
- 100 min for Port Alberni;
- 4 and 130 min for Bamfield; and
- 50 min for Port Renfrew.

These periods are in good agreement with typical periods for tsunami waves recorded at these stations (cf. Rabinovich et al. 2013).

Another specific feature of the f–t diagrams is a dramatic amplification of all frequencies at the time of the passing air pressure disturbances, as indicated in Figs. 10 and 12 by labels 1, 2, and 3. The sea level disturbance associated with AD1 is the most spectacular. After the air pressure disturbances crossed a given site, the sea levels kept oscillating for hours, whereas the atmospheric pressure oscillations stopped almost immediately. Also, in contrast to corresponding diagrams for sea level variability, the f–t diagrams for atmospheric pressure
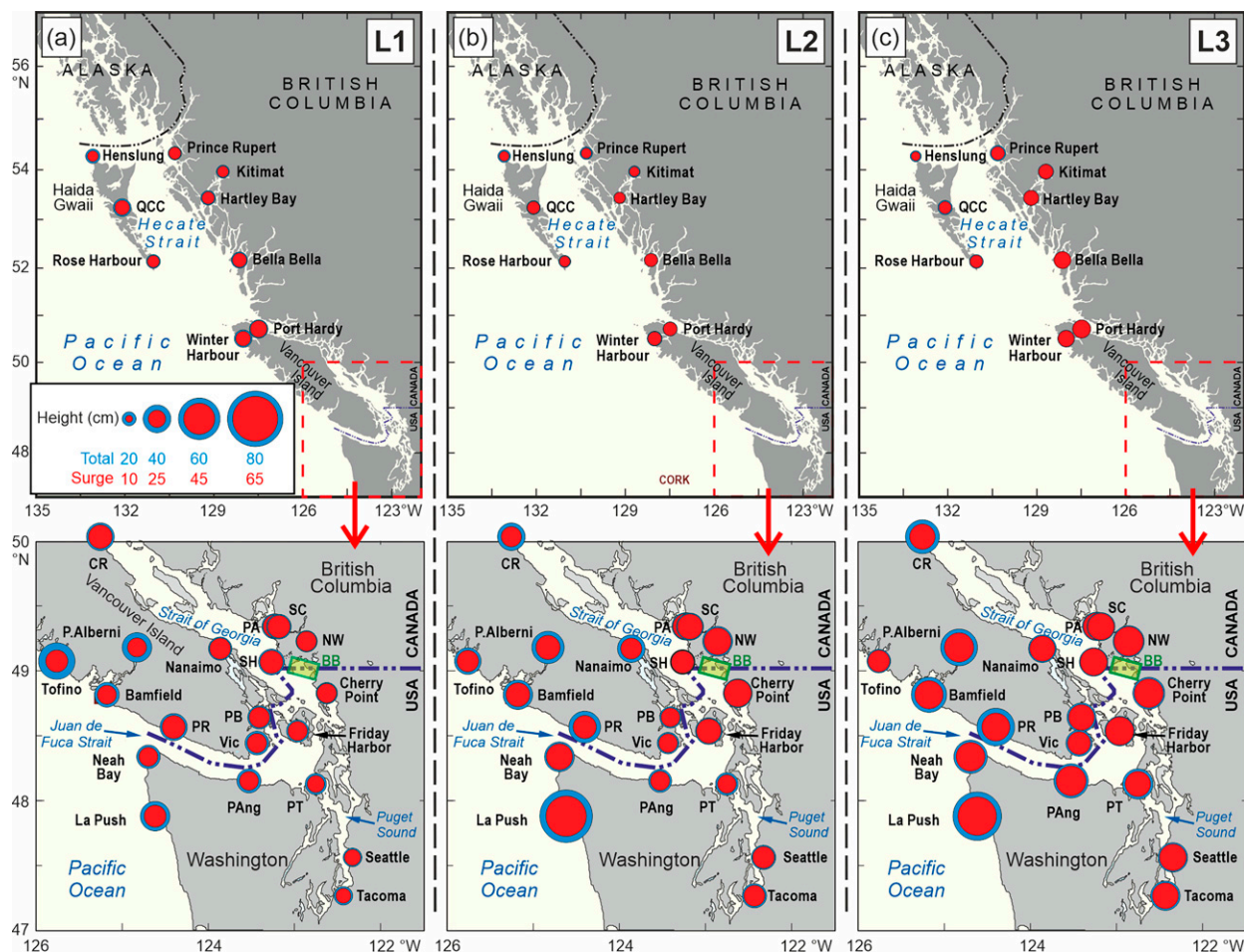
FIG. 9. Maps showing flood heights (relative to mean sea level) during 13–17 Oct 2016 along the coast of BC and WA associated with (a) L1 and AD1, (b) L2 and AD2, and (c) L3 and AD3. The size of the blue circles denotes the total height, and the size of the inner (red) circle denotes the height of the surge component. Abbreviations are as follows: QCC = Queen Charlotte City, CR = Campbell River, SC = Sandy Cove, PA = Point Atkinson, NW = New Westminster, SH = Sand Heads, PB = Patricia Bay, Vic = Victoria, PR = Port Renfrew, PT = Port Townsend; PAng = Port Angeles, and BB = Boundary Bay.

do not have specific "resonant" frequency bands of enhanced energy. In general, the *f–t* analyses support evidence for a strong sea level response to propagating atmospheric disturbances and to the high importance of local topographic resonance in the formation of hazardous floods. Storm-related IG waves with periods of <5 min are also an important factor amplifying high-frequency seiches at specific sites (e.g., Port Renfrew). We note that at some sites (e.g., Winter Harbour) the sea level started oscillating before the passage of AD1 (Fig. 12). Inspection of the air pressure time series from this location (Figs. 11 and 12) reveals that the onset of sea level oscillations coincided with the passage over the area of a series of air pressure waves, but they were much weaker than for AD1–AD3.

5. Offshore sea level oscillations

In addition to being recorded at coastal regions, the atmospherically induced sea level oscillations were measured by open-ocean NEPTUNE bottom pressure recorders. The BPRs have been used previously to examine tsunamis arriving at the BC coast, including the 2009 Samoa (Thomson et al. 2011), 2010 Chile (Rabinovich et al. 2013), 2012 Haida Gwaii (Fine et al. 2015), and 2018 Alaska-Kodiak (Wang et al. 2020) events. However, this is the first time that the offshore instrumentation has been used to investigate meteotsunamis seaward of the coast of Vancouver Island.

a. Oceanic response to atmospheric disturbances

There are significant differences between the coastal and deep-ocean sea level oscillations. While coastal tide gauges measure absolute changes in sea level, open ocean BPRs measure *the weight of the fluid column* (air plus water) above the instrument (cf. Rabinovich and Eblé 2015; Thomson and Fine 2021). The displacements of the free surface caused by steric sea level deviations or by the isostatic ocean response to the variations in air pressure do not change the column weight
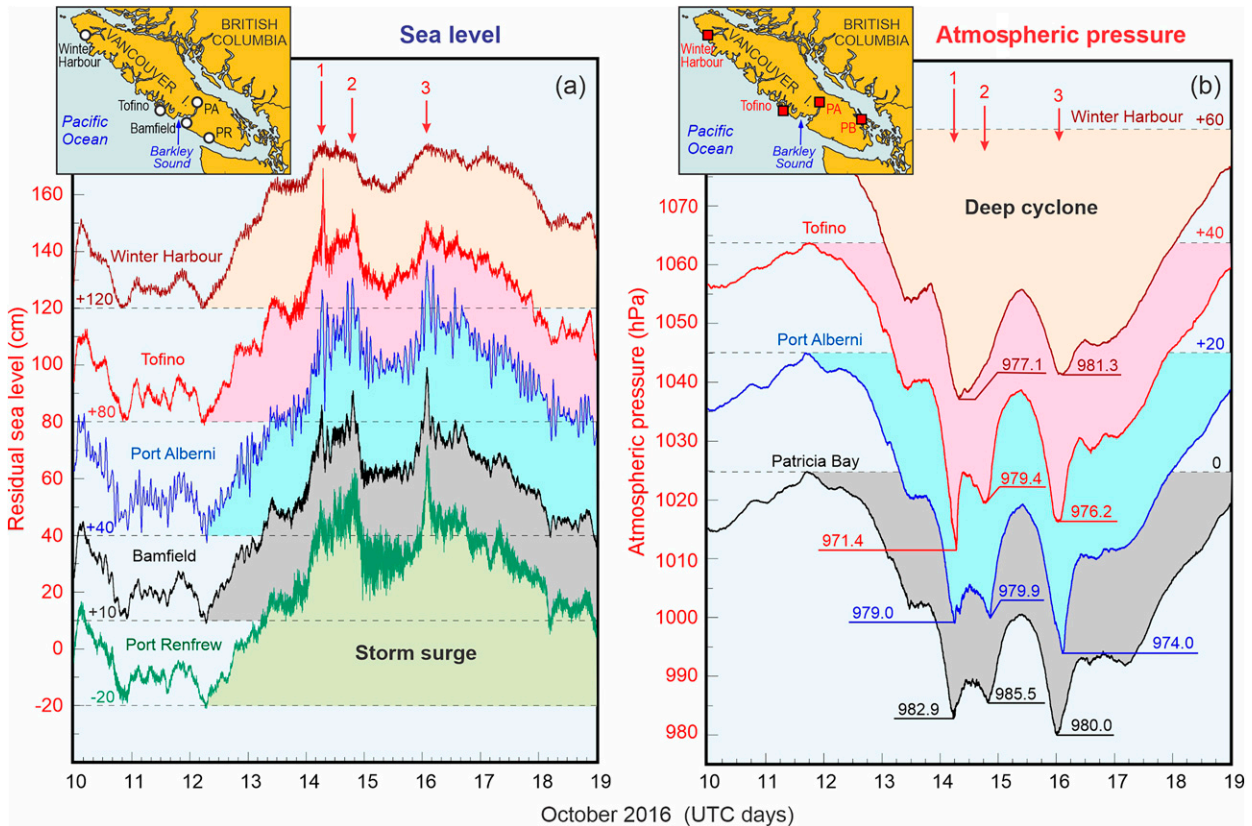
FIG. 10. (a) Residual (detided) sea level records at five CHS tide gauge stations along the outer coast of Vancouver Island for the period of 10–19 Oct 2016, and (b) simultaneous atmospheric pressure records at four CHS stations on Vancouver Island. For display purposes, the records are offset from one another; the corresponding vertical shifts are indicated along the left axis in centimeters for (a) and along the right axis in hectopascals for (b). The sea level rise associated with storm surges and the air pressure fall associated with three low pressure areas are denoted by shading. The red arrows labeled 1, 2, and 3 in (a) indicate the three consecutive sea level maxima (SL1, SL2, and SL3) associated with the L1, L2, and L3 lows [marked by red numbers in (b)] observed at these sites. The location of the stations is shown in the insets: PA = Port Alberni, PR = Port Renfrew, and PB = Patricia Bay.

and, therefore, are not recorded by BPRs. As shown by Fig. 13a, the instruments located in water depths of 380–2654 m did not record significant low-frequency variations, contrary to the low-frequency variations evident in the coastal records (Figs. 8 and 10). This means that the open-ocean sea level reaction to the variations in air pressure corresponded to isostatic "inverse barometer" response (i.e., a roughly 1-cm rise in sea level rise for a 1-hPa fall in air pressure). The exception is Folger Passage, the shallowest (96 m) and the closest to shore NEPTUNE station, where marked sea level rises were observed on 14–17 October. Three sharp peaks (corresponding to SL1, SL2, and SL3) were recorded at this site, the same as in the coastal records (Fig. 10a). SL3 was the highest, while SL1 the lowest (Fig. 12), similar to the shape and height of these peaks at Bamfield, the station nearest to Folger Passage (see Fig. 2). We assume that the major factor responsible for this nonstatic sea level rise at Folger Passage is an onshore wind combined with the dynamic effect of air pressure disturbances propagating over the shelf. This wind could also be partly responsible for the formation of the three enhanced sea level peaks.

High-frequency open-ocean sea level oscillations (high-passed with a 4-h KB filter) are shown in Fig. 13b. Tsunami-like waves are evident at Folger Passage, as well as at the two Barkley Canyon stations. All records in Fig. 13b reveal high-frequency oscillations beginning around noon local time on 13 October and lasting for three days. This "noise," which appears to be associated with storm-generated infragravity waves (cf. Rabinovich 2009), was highly intense at the exposed coastal station of Port Renfrew (Fig. 11a) but was weak at other coastal stations sheltered from the arriving storm waves.

We used the HF record at Folger Passage to estimate the wave amplitudes and peak values of HF sea level oscillations associated with atmospheric disturbances AD1, AD2, and AD3 passing over this station (Table 4). The same parameters were estimated for coastal stations, Bamfield and Tofino, located nearby (from Fig. 11a). HF sea level oscillations related to AD1 were the strongest and were clearly recorded at Folger Passage; 9 min later the maximum wave was observed at Bamfield and 33 min later at Tofino. The peak values at Folger Passage and Bamfield were similar (9.5 and 8.6 cm,

TABLE 3. Atmospheric pressure (P_a) minima and sea level maxima (ζ) during the October 2016 Songda event on the west coast of Vancouver Island. At some stations, similar extreme air pressure values were repeated several times within an interval of a few minutes.

Station	SL1 Variable	SL1 Time (UTC)	SL2 Variable	SL2 Time (UTC)	SL3 Variable	SL3 Time (UTC)
			Atmospheric pressure (minima; hPa)			
Patricia Bay	982.9	0520 14 Oct	985.5	1930 14 Oct	980.0	0005 16 Oct
Port Alberni	979.0	0557 14 Oct	979.9	2043 14 Oct	974.0	0243–0244 16 Oct
Bamfield (VS)	976.6	0642 14 Oct	976.9	2032 14 Oct	969.9	0254 16 Oct
Tofino	971.4	0639 14 Oct	979.4	1840 and 1846, 14 Oct	976.2	0039 16 Oct
Winter Harbour	977.1	0744 14 Oct	—	—	981.3	0217–20 16 Oct
			Sea level (maxima; cm)			
Port Renfrew	34.9	0551 14 Oct	45.8	1958 14 Oct	54.2	0215 16 Oct
Bamfield	37.6	0628 14 Oct	42.6	1919 14 Oct	50.8	0159 16 Oct
Port Alberni	42.6	0634 14 Oct	46.7	1910 14 Oct	53.1	0200 16 Oct
Tofino	52.6	0701 14 Oct	38.3	1907 14 Oct	34.3	0140 16 Oct
Winter Harbour	24.9	0703 14 Oct	—	—	24.3	0232 16 Oct

respectively), while at Tofino the wave was much larger (18.2 cm). The induced oscillations at Bamfield/Folger Passage and at Barkley Canyon were in antiphase, a result that is examined in more detail in section 5b.

The wave amplitudes recorded at Folger Passage during passage of events AD2 and AD3 were 5.5–6.0 cm (i.e., slightly weaker than during AD1) and were of approximately the same height as at coastal stations Bamfield and Tofino

(3.6–7.9 cm). One of the most noteworthy features was the arrival times of peak values. For the HF sea level oscillations linked to AD2, these values were comparable for all three stations (Bamfield, Tofino, and Folger Passage), while the sea level HF peak associated with AD3 was first observed at Tofino, then 20 min later at Bamfield and then 9 min later at Folger Passage (Table 4). This means that the three HF sea level disturbances had significantly different propagation
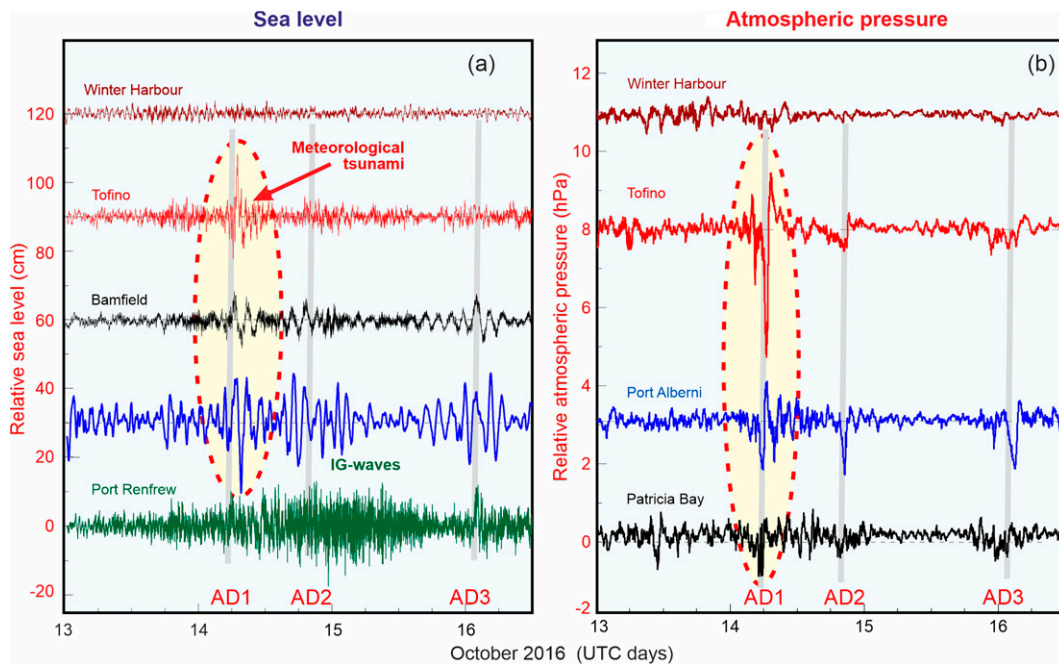

FIG. 11. (a) Detided and high-pass-filtered (with a 4-h KB window) records for five CHS tide gauge stations, and (b) high-pass-filtered records of air pressure at four CHS AP stations on Vancouver Island for the period 13–16 Oct 2016. Locations of the stations are shown in the insets to Figs. 10a and 10b. To improve the presentation, the records are offset from one another. The meteotsunami of 14 Oct and the air pressure disturbance (AD1) that generated it are indicated by the shading inside the ovals. Red labels AD1, AD2, and AD3 and thick gray lines in (a) and (b) indicate the three consecutive atmospheric disturbances propagating over these sites.
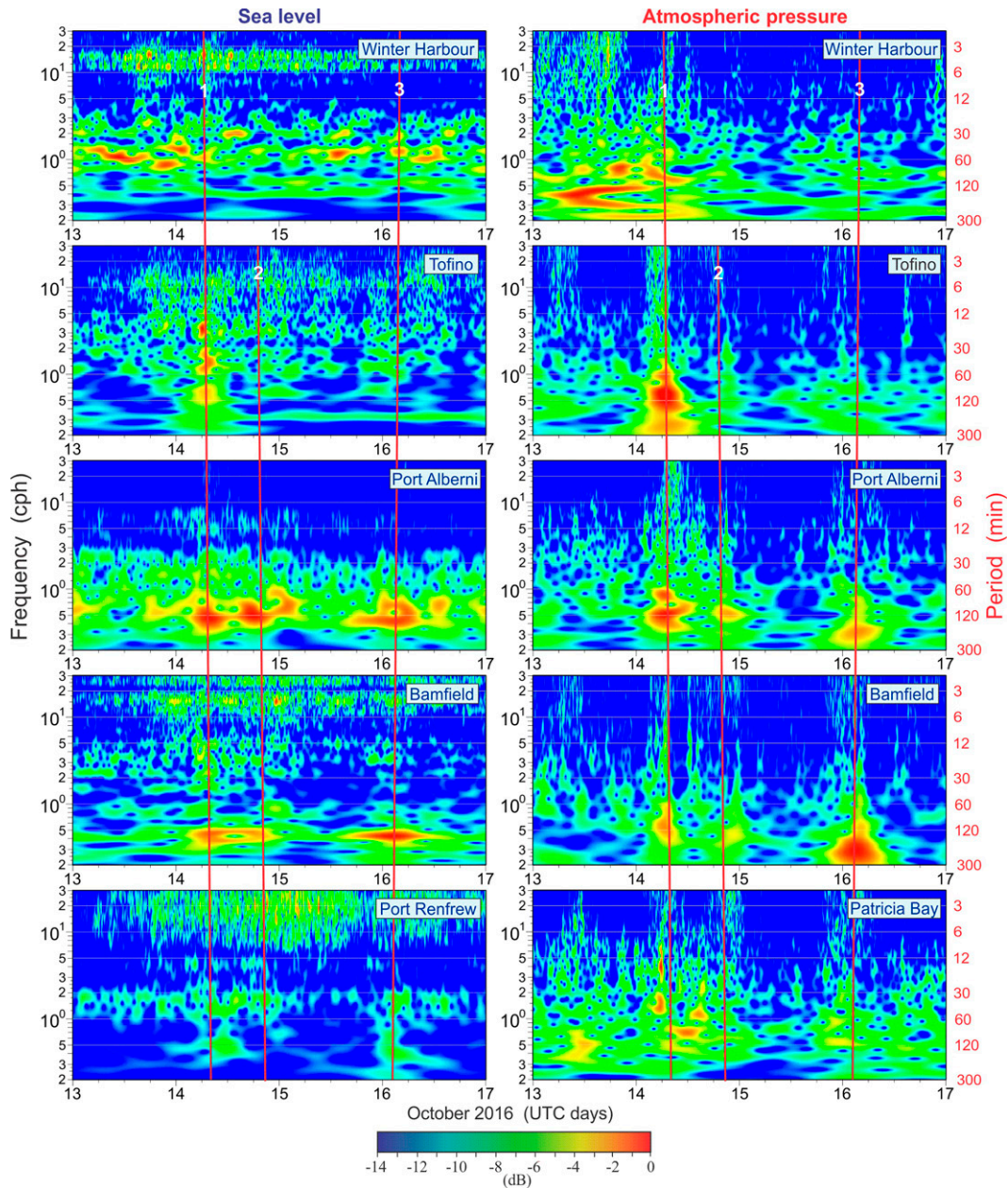
FIG. 12. Frequency–time plots (*f–t* diagrams) for (a) the five CHS sea level records shown in Fig. 11a, and (b) the four CHS air pressure records shown in Fig. 11b plus an additional record from the Bamfield VS school network station. Red vertical lines with labels 1, 2, and 3 indicate three major atmospheric disturbances (AD1, AD2, and AD3) that passed over Vancouver Island and corresponding sea level responses.

directions relative to the station locations, as did air pressure disturbances AD1–AD3, which likely caused these oscillations (Table 2; Fig. 6b).

Further properties of recorded offshore long waves are obtained using *f–t* analysis of the ONC NEPTUNE records (Fig. 14). The low-frequency oscillations with periods of ~125–135 min at Folger Passage and Barkley Canyon-380 appear to be associated with the strong intensification of the fundamental eigenmode within Barkley Sound during the

extreme events. Significant oscillations with this period are regularly observed at Bamfield located near the entrance to the sound (see Fig. 2 for location) (cf. Rabinovich and Stephenson 2004; Rabinovich et al. 2013). A further reason for amplification of the oscillations is that the atmospheric forcing had approximately the same period as the resonant oceanic motions; (see the AP *f–t* plots for Bamfield, Port Alberni, and Tofino in Fig. 12).

Additional weaker sea level oscillations with periods of 30–60 min appeared at almost all offshore stations (Fig. 14)
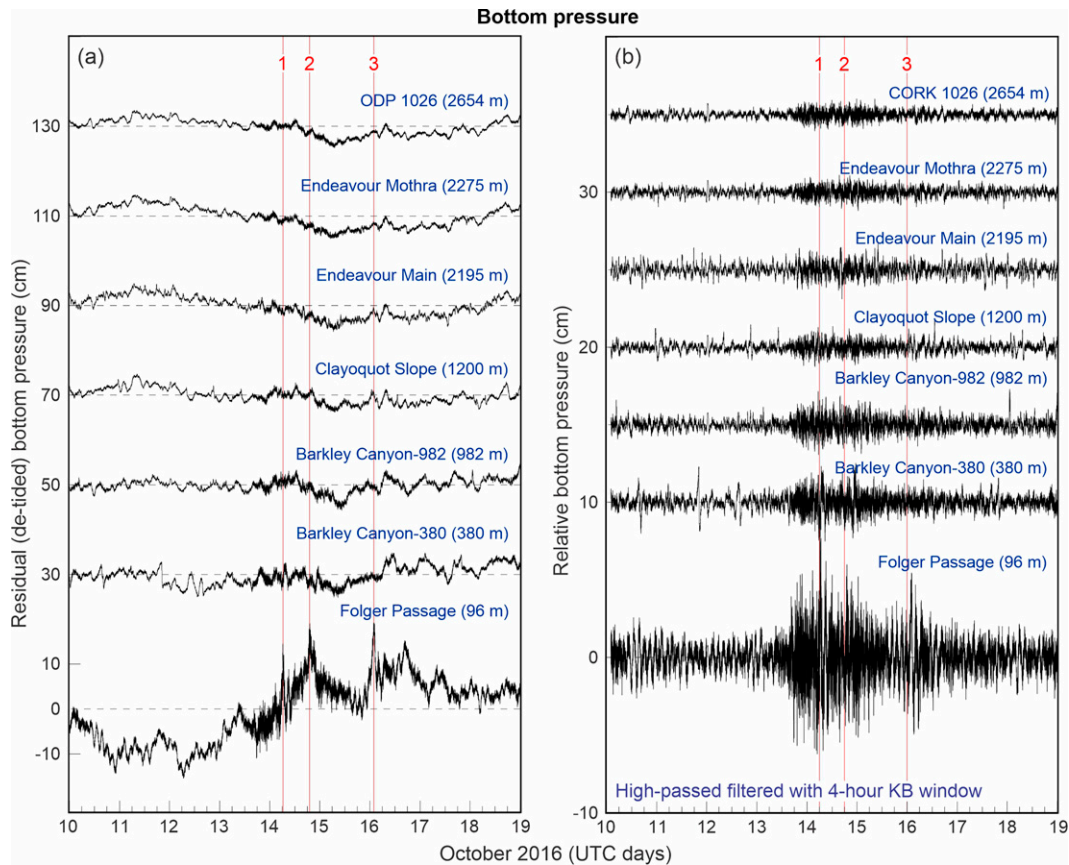
FIG. 13. (a) The residual (detided) bottom pressures measured during the Songda event of 12–16 Oct 2016 by the NEPTUNE Canada cabled array located seaward of southwestern Vancouver Island. (b) As in (a), but following high-pass filtering using a 4-h KB window. Red vertical lines indicate three major HF atmospheric disturbances (AD1, AD2, and AD3) that passed over Vancouver Island.

and were most likely due to propagating atmospheric disturbances with these periods, as seen in the air pressure f-t diagrams, especially at Patricia Bay (Fig. 12). A "cloud" of high-frequency oscillations with periods of $<$6–8 min is a prominent feature of all offshore sea level records during the storm. These periods are typical of IG-waves associated with the storm; their widespread appearance over the shelf and continental slope indicates that they were "forced" (or "locked") IG waves that were highly correlated with the group structure (trains) of wind waves (Aida et al. 1970;

Gerritsen and Van Heteren 1984; Huntley and Kim 1984; Webb et al. 1991).

b. Standing waves on the shelf of Vancouver Island

Figure 15 shows sea level oscillations at Bamfield and at two close-proximity offshore NEPTUNE stations–Folger Passage and Barkley Canyon-380–recorded during SL1. Low-frequency oscillations at Bamfield and Folger Passage are similar, while those at Barkley Canyon are the "mirror image"—that is, they are exactly in *antiphase* with troughs in the Barkley Canyon

TABLE 4. Bottom pressure and sea level extrema (peaks) of high-frequency oscillations recorded on and off the west coast of Vancouver Island during the mid-October 2016 sea level maxima (SL1, SL2, and SL3). Values in parentheses (e.g., 14 Oct) denote the day and month of the event in 2016.

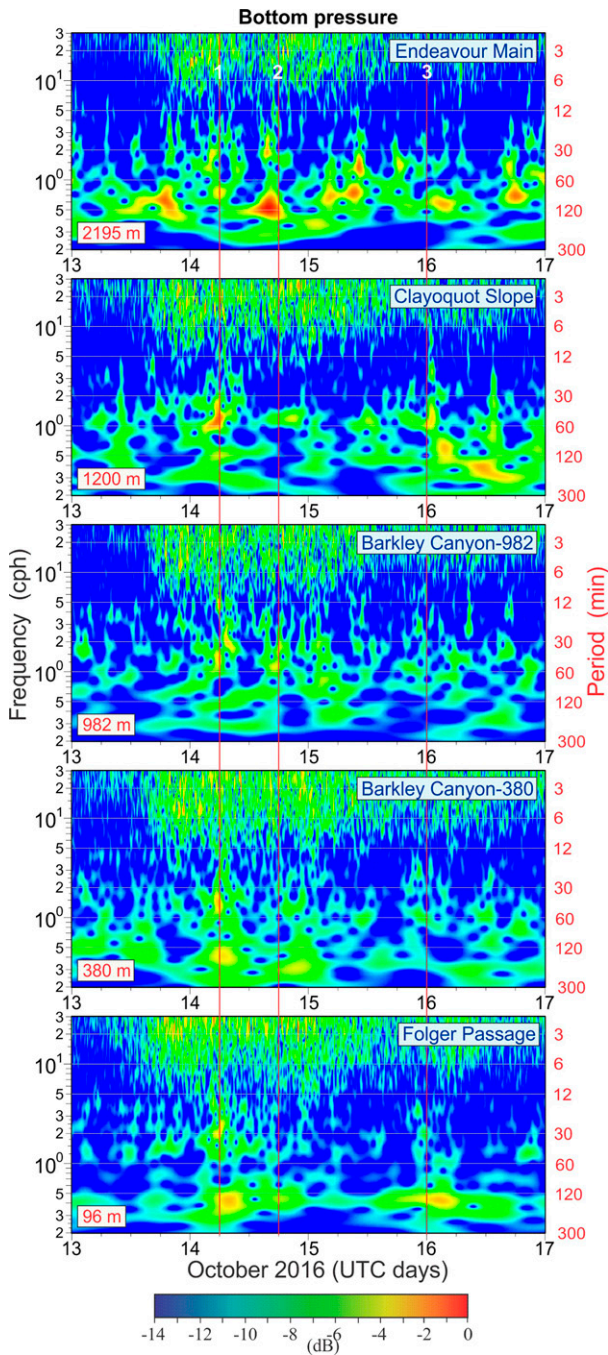| Station	Depth (m)	SL1 (14 Oct)		SL2 (14 Oct)		SL3 (16 Oct)	
		ζ (cm)	Time (UTC)	ζ (cm)	Time (UTC)	ζ (cm)	Time (UTC)
Folger Passage	96	9.5	0619	6.0	1911	5.5	0207
Bamfield	0	8.6	0628	5.7 6.4	1856, 1919	7.9	0159
Tofino	0	18.2	0701	6.0	1907	3.6	0139

FIG. 14. The *f–t* diagrams for five NEPTUNE BPR records shown in Fig. 13. The two deepest stations, Endeavour Mothra and CORK ODP 1026, are not shown because they are similar to the Endeavour Main record. Red vertical lines labeled 1, 2, and 3 indicate the times of three major atmospheric disturbances (AD1, AD2, and AD3) that passed over Vancouver Island.

record corresponding to sea level crests at Folger Passage and Bamfield, and vice versa. To further quantify this effect, we low-pass filtered these three records with a 20-min KB window and decimated the filtered records to 10-min time steps (Fig. 15).

FIG. 15. The residual and high-pass-filtered (4-h KB window) bottom pressure records at the NEPTUNE-ONC stations (top) Barkley Canyon (380 m) and (middle) Folger Passage (96 m) located offshore of southwestern Vancouver Island, along with the sea level record at (bottom) Bamfield, during SL1 of 14 Oct 2016. Red curves are the same records but additionally low-pass filtered with a 20-min KB window and decimated to 10-min intervals.

Our analysis yielded the following empirical relationships between sea level at Bamfield Y_{Bam} and the open-ocean records at Folger Passage X_{FP} and Barkley Canyon-380 X_{BC}:

$$Y_{Bam} = 1.12 X_{FP} \pm 0.10 \quad (R^2 = 0.83) \quad \text{and}$$

$$Y_{Bam} = -2.13 X_{BC} \pm 0.48 \quad (R^2 = 0.52). \tag{2}$$

These findings indicate that the 125–135-min ocean waves observed during SL1 (see Figs. 14 and 15) were likely *standing waves*, with a nodal line located between Folger Passage and Barkley Canyon-380. Kovalev et al. (1991) observed a similar effect of standing long waves induced by a storm on the west shelf of the Kamchatka Peninsula.

The system of the waves formed on the southwestern shelf of Vancouver Island on 14 October 2016 can be described by a simple anaytical model. Consider the sea level displacement $\zeta(x, y; t) = \zeta(x)e^{i(\omega t - ky)}$, where (x, y) are Cartesian coordinates. For convenience we specify that the x axis is positive in the offshore direction and the y axis is positive in the along-shore direction (positive equatorward), t is time, ω is the
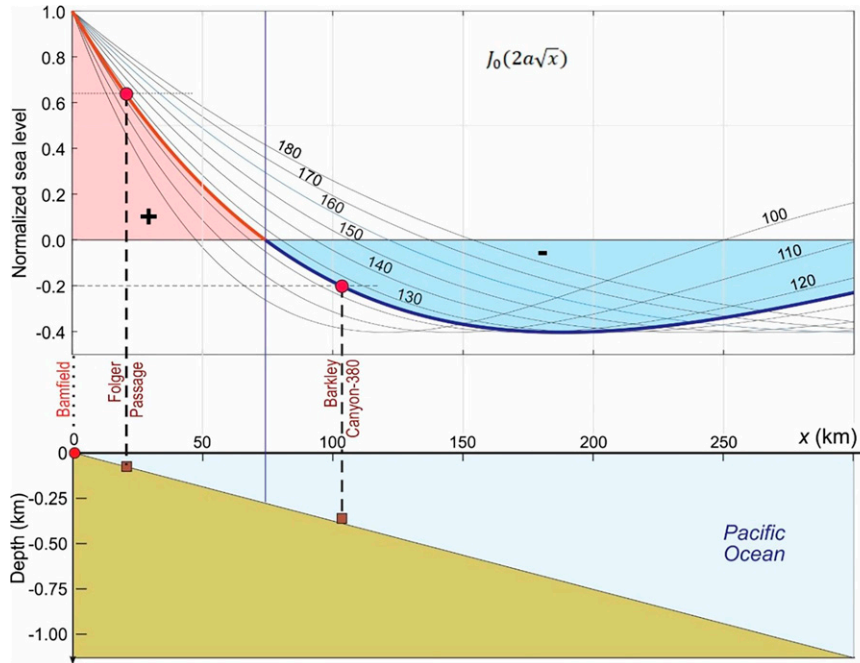
FIG. 16. Theoretical solutions for standing long waves over a linear slope (Lamb 1945), approximating the southwestern shelf of Vancouver Island, showing the locations of the coastal tide gauge at Bamfield (depth 0 m) and the bottom pressure NEPTUNE ONC stations Folger Passage (96 m) and Barkley Canyon (380 m). The thin black curves describe the solutions of Eq. (5) for various values of parameter a, corresponding to different wave periods, 100, 110, 120, …, 180 min. The thick red/blue curve denotes the period $T = 125$ min.

angular frequency, and k is the wavenumber. Then the cross-shore structure for water depth $h = h(x)$, uniform in the along-shore direction, has the form (cf. LeBlond and Mysak 1978)

$$\zeta''(x) + \left[\frac{h'(x)}{h(x)}\right]\zeta'(x) + \left[\frac{\omega^2}{gh(x)} - k^2\right]\zeta = 0, \quad (3)$$

where prime $\equiv d/dx$. For a linear sloping depth profile, $h(x) = \alpha x$, Eq. (3) becomes

$$\zeta''(x) + \frac{1}{x}\zeta'(x) + \left(\frac{a^2}{x} - k^2\right)\zeta = 0, \quad (4)$$

where $a^2 = \omega^2/(\alpha g)$. If $k \neq 0$, then Eq. (4) describes a family of *trapped edge waves* propagating alongshore in both directions (Eckart 1951). A specific situation is when $k = 0$ (i.e., for waves traveling normally to the coast). In that case, Eq. (4) has the solution (Lamb 1945, section 186):

$$\zeta(x) = AJ_0(2a\sqrt{x}), \quad (5)$$

where A is the wave amplitude and J_0 is the zeroth-order Bessel function. Equation (5) describes a system of *standing waves* with nodal lines parallel to the shore. This solution perfectly explains the observed structure of long-period waves on the southwestern shelf of Vancouver Island on 14 October 2016 (Fig. 16).

The offshore station Folger Passage ($h = 96$ m) is located 20.6 km from Bamfield; Barkley Canyon-380 ($h = 380$ m) is 103.5 km from Bamfield and approximately 83 km from Folger Passage. Assuming that at Bamfield $x = 0$, $h(0) = 0$, we can approximate the depth profile as $h(x) = \alpha x = 0.00367x$ (m). Using this parameter of α, we computed the normalized sea level displacement, $\zeta(x)$ for $A = 1.0$ and different wave periods $T = 2\pi/\omega$: 100, 110, 120, …, 180 min (Fig. 16). We found that the best agreement with the observations is achieved when $T = 125$ min (the thick red/blue line in Fig. 16). For this particular period, we note two things.

1) Equation (5) describes a standing wave with a nodal line located at $x = 74$ km (i.e., between Folger Passage and Barkley Canyon). Therefore, the corresponding oscillations (with $T = 125$ min) at these two stations should be in antiphase, in exact agreement with the observations.

2) The ratio of the theoretical amplitudes at Folger Passage and Barkley Canyon-380, $A_{\text{FP}}/A_{\text{BC}} \sim 0.31$, is also in good agreement with the observed ratio (Fig. 16).

This reveals that a simple analytical model describes the character of the wave field during SL1. Standing waves on this shelf were also observed during events SL2 and SL3, but they were less well defined, probably because the directions of the atmospheric disturbances were not optimal.

6. Numerical modeling of the oceanic response

The extreme HF sea level oscillations observed during SL1 were numerically simulated using an ocean model based on the depth-integrated shallow-water equations, ignoring the Coriolis effect and all nonlinear terms, except bottom friction. The equations of horizontal motions [Eq. (6a) and (6b)] and continuity [Eq. (7)] are then as follows:

$$\frac{\partial U}{\partial t} = -\frac{C}{h^2} U \sqrt{U^2 + V^2} - gh\frac{\partial \eta}{\partial x}, \tag{6a}$$

$$\frac{\partial V}{\partial t} = -\frac{C}{h^2} V \sqrt{U^2 + V^2} - gh\frac{\partial \eta}{\partial y}, \quad \text{and} \tag{6b}$$

$$\frac{\partial \eta}{\partial t} = -\frac{\partial U}{\partial x} - \frac{\partial V}{\partial y} + \frac{\partial \zeta_A}{\partial t}, \tag{7}$$

where t is the time, (x, y) are the Cartesian coordinates in the eastward and northward directions, respectively, (U, V) are the depth-integrated components of velocity in the (x, y) directions, $h = h(x, y)$ is the depth, g is the acceleration of gravity, η is the sea level adjusted for the equilibrium inverse barometric (IB) effect, ζ_A is the nonequilibrium sea level, and C is a nonlinear bottom friction coefficient (set to 0.0025, a commonly accepted value). The sea level response to the air pressure forcing appears as a time derivative in the continuity Eq. (7). This model code had been developed by I. Fine [Institute of Ocean Sciences (IOS), Sidney, BC] and has been successfully used in various meteotsunami modeling experiments (cf. Šepić et al. 2015, 2018) including simulations of meteotsunamis in Juan de Fuca Strait and the southern Strait of Georgia on the BC–WA coast (Rabinovich et al. 2021).

At the coastal boundary G, we assume that there is a vertical wall with zero normal flow:

$$U_n = 0 \text{ on } G, \tag{8}$$

while on the open boundary Γ, we used the radiation condition

$$\frac{\partial \eta}{\partial n} - \frac{1}{c}\frac{\partial \eta}{\partial t} = \frac{\partial \zeta_A}{\partial n} - \frac{1}{c}\frac{\partial \zeta_A}{\partial t} \text{ on } \Gamma, \tag{9}$$

where $c = (gh)^{1/2}$ is the longwave speed and n is directed perpendicular to the boundary.

An explicit finite-difference method is used to solve Eqs. (6) and (7) with boundary conditions of Eqs. (8) and (9). We applied the Arakawa C-grid approximation and used a grid with 9 arc s × 9 arc s (~180 m × 270 m) resolution (Fig. 17a). The model domain had 1099 × 419 grid points. Within the constraints of the Courant–Friedrichs–Lewy criterion, the time step Δt was chosen to be 1.1 s.

The model was used to reproduce the high-frequency sea level oscillations forced by the passage of disturbance AD1 over the area. Our prime consideration was reproducing the knife-like oscillation recorded at Tofino (Fig. 11a) and the standing waves recorded on the southwestern shelf of Vancouver Island (Fig. 15). Thus, we forced the model with the AD1 time series measured at Tofino (Fig. 17b). The disturbance was assumed to propagate over the domain with speed

U = 21.1 m s^{-1} in direction θ = 130.7° (Table 2), with a cross-propagation width defined by Eq. (1) and values taken from Table 2.

The maximum modeled sea level oscillations over the entire domain and over the two areas of interest (Tofino and Barkley Sound) are shown in Fig. 17. The highest oscillations, reaching up to 60-cm height, are closely reproduced for the western coast of Barkley Sound, Alberni Inlet, the Tofino area, and for the coast of Vancouver Island northwest of Tofino. As for offshore areas, the highest displacements, up to 40 cm in height, are obtained for those parts of the Vancouver Island shelf that were oriented parallel to the direction of atmospheric disturbance propagation and for which the speed of long ocean waves matched the speed of the AD1 disturbance.

Comparison of simulated waveforms and recorded high-pass-filtered sea levels at the coastal and offshore stations (Fig. 18) shows that the model simulates the main features of the observed high-frequency sea level oscillations. The agreement for Tofino is remarkably good in that the model reproduces the exact shape and period of the observed sea level oscillations and gives only slightly smaller heights (modeled = 26.8 cm; measured = 31.1 cm). The fact that agreement is the best at Tofino is not surprising since the model was forced with the air pressure time series measured at this station. The agreement for other stations, in particular, for Bamfield and Port Alberni, is also acceptable (Fig. 18, left), both in terms of timing and amplitude, but slightly diminished in wave period (~110 min modeled vs ~120 min observed). Because of this difference in period, phase matching is lost after the first two oscillations. This disagreement appears to be due to an insufficient grid resolution for the model domain and to the absence of wind forcing in the model.

As for the offshore region, the model successfully reproduces the standing waves observed on the Vancouver Island shelf (Fig. 18; right). There is a small mismatch between the onset time of the modeled and observed oscillations at Barkley Canyon-380, and the period of the oscillations (the modeled periods are shorter than measured), but otherwise the agreement is close. Once the first ocean waves have passed, a standing wave, characterized by antiphase oscillations, is formed between offshore Barkley-Canyon-380 and the coastal (near-coastal) stations. These waves are clearly present in the measurements and the model (Figs. 15 and 18). The mismatch at Barkley Canyon-380 is likely due to the closeness of this station to the model domain boundary, but also possibly to the fact that our coastal air pressure measurements do not satisfactorily reflect the air pressure oscillations that passed over this area (the closest air pressure measurements are from Bamfield, some 30 km to the northeast). In this regard, our study is not alone. One of the key limitations of all numerical meteotsunami simulations that are based on actual atmospheric input data is the limited spatial resolution of these data; it is important to have not only 1-min time resolution but also 1–2-km spatial resolution. To circumvent this problem, Titov and Moore (2021) used radar data to numerically simulate the meteotsunami of 13 June 2013 on the U.S. East Coast. However, as the authors indicated, "more research is needed for testing the approach and developing a
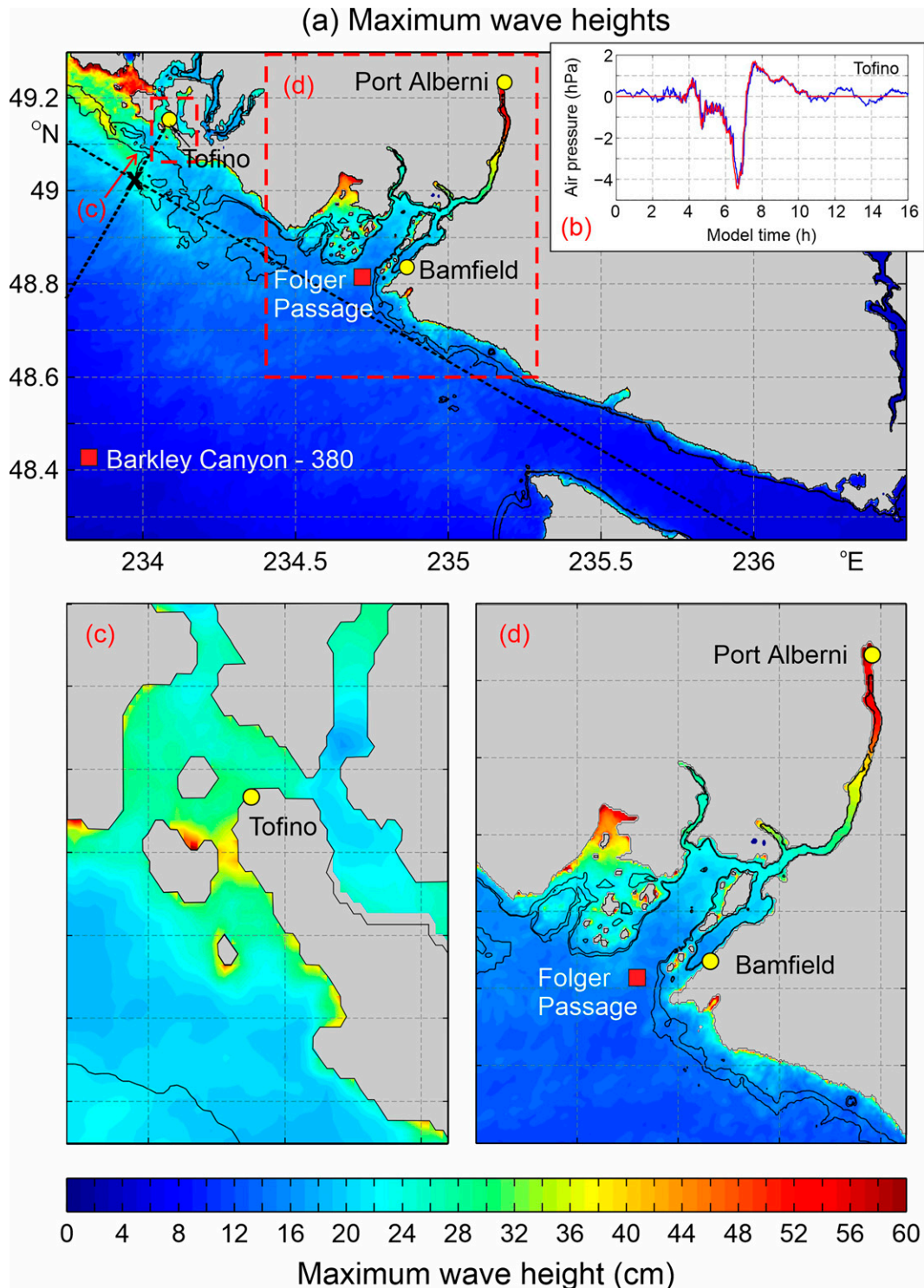
FIG. 17. (a) Maximum simulated wave heights over the model domain; (b) the recorded air pressure time series at Tofino (blue) and the slightly smoothed series that was used for the model forcing (red). Maximum simulated wave heights are for the (c) Tofino and (d) Barkley Sound regions. Black contours in (a), (c), and (d) encircle areas for which long wave speed is in the range of 20–22 m s^{-1}. Dashed lines in (a) mark cross sections used in Fig. 19, below.
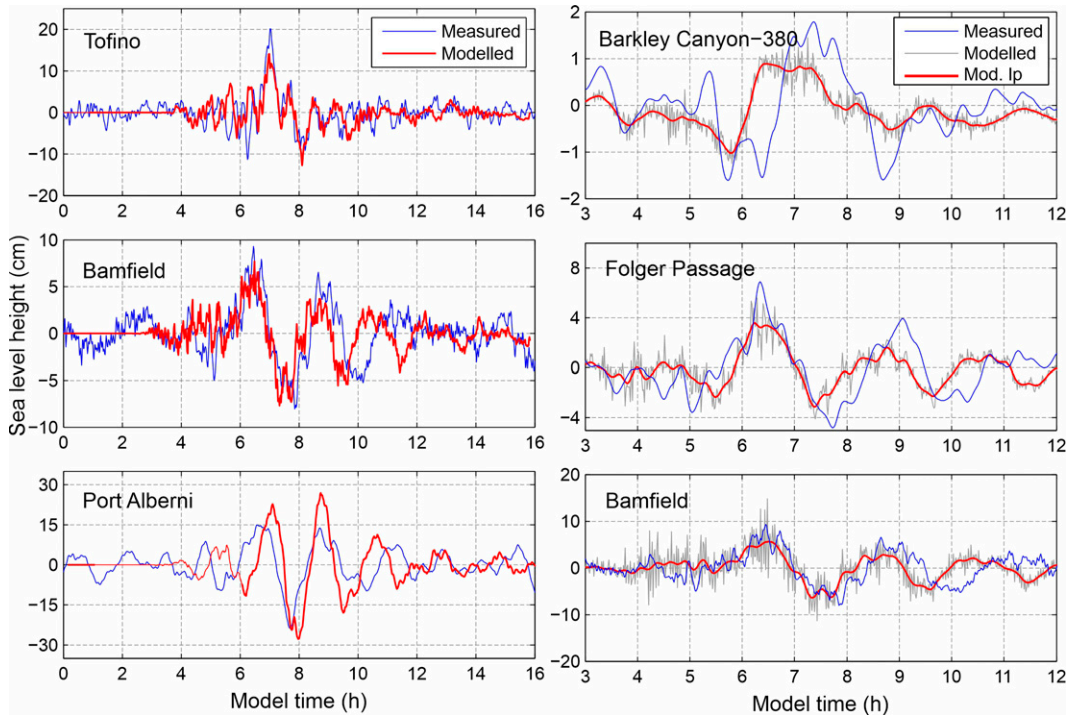
FIG. 18. Observed (blue) and simulated (red) sea levels at (left) coastal stations Tofino, Bamfield, and Port Alberni and (right) offshore stations Barkley Canyon-380, Folger Passage, and Bamfield. All observed series were high-pass filtered with a 4-h KB window. In addition, both simulated and observed series on the left were low-pass filtered with a 5-min KB window, and those on the right were low-pass filtered with a 20-min KB window.

robust capability." In our case, the VS network provided us with atmospheric data that had much higher spatial resolution than is normally available (see insets in Fig. 2), Even then, the spatial resolution of data in the area of Tofino/Banfield/Port Alberni was quite poor, which contributed to the mismatch mentioned above.

Sensitivity tests were conducted to specify the mechanisms of generation and growth of long ocean waves. The ocean model was forced with air pressure disturbances of the same shape and direction as in the original experiment but were allowed to propagate over a range of speeds (19, 21, 23, and 25 m s^{-1}) (Fig. 19). It appears that there are two distinct mechanisms responsible for the amplification of long waves on the southwestern shelf of Vancouver Island: the first mechanism is related to along-track increase of the wave heights due to Proudman resonance and the second mechanism to shoreward increase in ocean wave heights due to shoaling effects. The strongest along-track increases in wave heights occurred at ~100 km offshore for the atmospheric disturbance propagating with a speed of 25 m s^{-1}, and at ~25 km for atmospheric disturbances propagating with speeds of 21 and 23 m s^{-1}—that is, precisely over those depths at which the corresponding Froude number,

$$\mathrm{Fr} = U/c, \tag{10}$$

is close to unity: Fr ~ 1.0. Here, U is the atmospheric disturbance speed, and $c = (gh)^{1/2}$ is the longwave speed. Proudman resonance, which occurs when $U \sim c$ and Fr ~ 1, plays a key role in the formation of significant meteotsunamis (cf. Šepić et al. 2015; Rabinovich 2020; Heidarzadeh et al. 2020). The results of our numerical experiments demonstrate that the speed of 21 m s^{-1}, which was found to be the actual speed of disturbance AD1 (see Table 2), is the speed that produces the strongest sea level response on the shallow shelf off Vancouver Island (Fig. 19), and that this response arises from a combination of Proudman resonance and shoaling effects (cf. Šepić et al. 2015), reaching heights of ~30–40 cm in the area of Tofino.

7. Discussion and conclusions

The series of three strong low pressure systems, including the tail end of Typhoon Songda, that impacted the southwest coast of British Columbia and northwest Washington, Vancouver Island, Juan de Fuca Strait, and the southern Strait of Georgia in mid-October 2016 generated three different types of significant sea level oscillations: 1) storm surge, 2) seiches and meteotsunamis, and 3) infragravity waves. Storm surges alone exceeded 1 m in some parts of the study region. At various sites, different types of oscillations prevailed, but the strongest effects were caused by the superposition of the three forms of oscillation. The importance of such cumulative impacts was discussed in detail by Thomson et al. (2007), Heidarzadeh and Rabinovich (2021), and Medvedev et al. (2022). We find that the highest risk for flooding for given
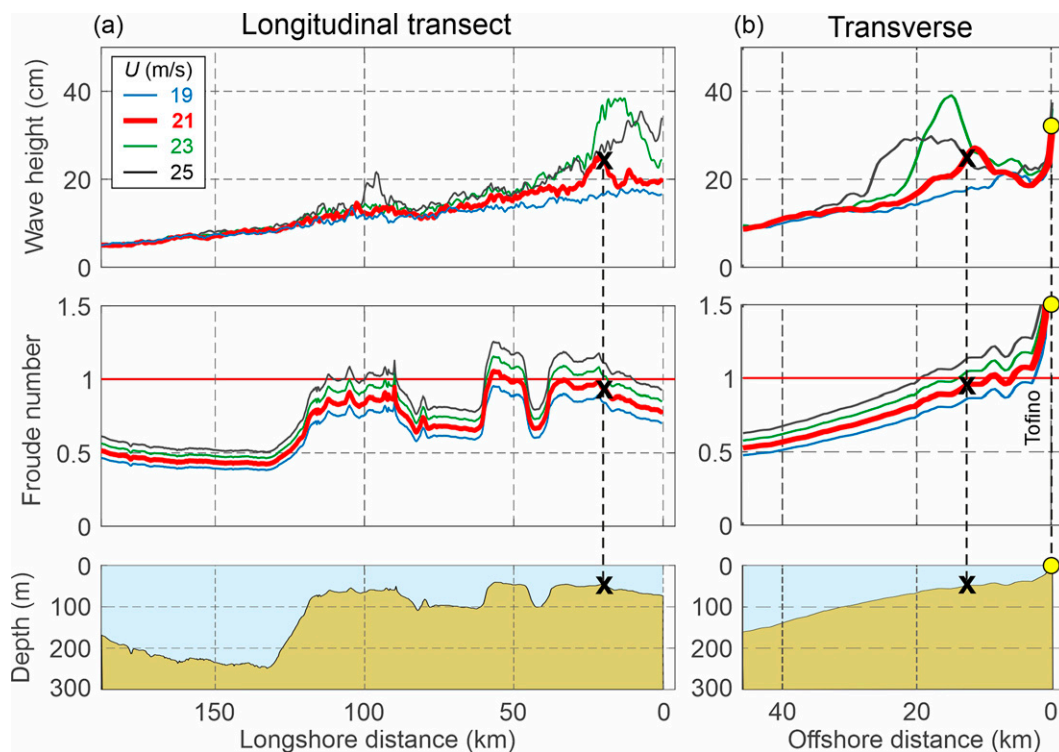
FIG. 19. (top) Maximum modeled wave height and (middle) Froude number, both for a range of speeds for the atmospheric pressure disturbances, along with (bottom) the depth profile, all plotted along the (a) longitudinal and (b) transverse transects marked in Fig. 17a. The X marks the intersection of the longitudinal and transverse transects.

coastal locations is mainly related to the combination of shelf topography and coastline geometry that create favorable resonant wave conditions and form "hot spots" (e.g., Šepić and Rabinovich 2014), that is, sites with the highest expected sea level response to the atmospheric forcing.

Our examination of the extreme sea level oscillations generated by the atmospheric disturbances that crossed the British Columbia–WA coast in October 2016 is based on extensive oceanic and meteorological datasets, including tide gauge data from the CHS and NOAA, offshore bottom pressure measurements from ONC and high-resolution air pressure/wind data from a network of 171 (of 182) school-based weather stations located in southern BC. The sea level and weather data are complemented with data from multiple CHS and NOAA meteorological stations. These data allowed us to provide a detailed tracking of the atmospheric disturbances responsible for the observed sea level oscillations. A particularly noteworthy phenomenon was observed on the oceanic side of Vancouver Island, where the tide gauge record at Tofino indicated a sharp, knife-like 40-cm increase in sea level with a peak on 14 October 2016 that we have identified as a meteotsunami. Similar but less sharp sea level peaks were observed at Bamfield, Port Alberni, and Port Renfrew located nearby. During the next 1.5 days, two other abrupt tsunami-like events occurred in this region. The common feature of all these extreme peaks was that they were superimposed on a pronounced sea level rise associated with a major storm surge

that lasted for almost five days. The cumulative effect of the low-frequency storm surge variations and high-frequency oscillations associated with locally generated meteotsunamis and infragravity waves strongly amplified the coastal oceanic response.

In the open ocean, the strongest effect was observed at Folger Passage, the shallowest (96 m) ONC station and the closest to the shore off the entrance to Barkley Sound. A significant sea level rise was observed in Folger Passage during 14–17 October, with the same three sharp peaks that were recorded at nearby coastal stations. It appears that the major factor responsible for this nonisostatic sea level rise was the onshore wind, combined with the dynamic effect of fast-moving atmospheric disturbances. The data from numerous meteorological stations enabled us to define the propagation features of the air pressure disturbances, to estimate precisely their speeds, directions, and other parameters, and to construct an effective numerical model describing the physical properties of forced sea level oscillations at both the coast and offshore.

The f–t diagrams for sea level oscillations for the stations located on the outer coast of Vancouver Island revealed well-defined, relatively narrow frequency bands of markedly amplified energy. The stability and persistent character of these high-frequency oscillations throughout the entire study period indicate that the oscillations were associated with the oceanic eigen (resonant) periods for the sites: 4–5, 30, and 50 min for Winter Harbour; 20, 48, and 100 min for Tofino; 100 min for

Port Alberni; 4 and 150 min for Bamfield; and 50 min for Port Renfrew. Similar periods were identified at these sites during several seismically generated tsunami events that arrived at these areas from the open Pacific (cf. Rabinovich et al. 2013, 2019).

Another noteworthy feature of the sea level and air pressure f–t diagrams is the marked amplification of all frequencies at the time of the extreme events. The difference between these diagrams is that after the air pressure disturbances passed over the respective sites, the sea levels kept oscillating for several hours, whereas the atmospheric pressure oscillations, which mostly had periods between 40 min and 3 h, stopped almost immediately. In contrast to sea levels, the f–t diagrams for atmospheric pressure do not show specific "resonant" frequencies or corresponding enhanced energy. This means that the relatively broad spectrum of the air pressure forcing leads to distinct local responses for each tide gauge site. In general, the f–t analyses confirm significant sea level responses to the passing atmospheric disturbances and the major importance of local resonant topographic properties in determining flood risk for individual sites.

No pronounced high-frequency oscillations were observed in the southern Strait of Georgia, including the broad Boundary Bay region. It appears that Juan de Fuca Strait strongly attenuates the waves arriving from the open ocean, with an added sheltering effect by the San Juan Islands. In addition, there was no local generation of waves within the Strait of Georgia because atmospheric disturbances either did not pass over the area (as in the case of disturbance AD1) or had significantly weakened by the time that they had reached the strait (as in the cases of AD2 and AD3). In contrast, the storm surges (i.e., long-period motions) that accompanied the high-frequency motions were substantial and slightly amplified relative to those along the open coast off Vancouver Island. One of the highest storm surge heights (93 cm relative to the undisturbed sea level) was observed at New Westminster in the southern Strait of Georgia.

One other important aspect of this study is that it appears to be the first time that such an extensive set of instruments, including coastal, open-ocean, and high-resolution weather stations, has been used to examine atmospherically induced sea level oscillations. In particular, we were able not only to estimate the direction and speed of propagating atmospheric disturbances, but also to track their evolution and evaluate important disturbance parameters, including the cross-propagation width. This gives us insight into the scales and physics of poorly known mesoscale atmospheric disturbance responsible for the formation of meteotsunamis, while at the same time providing important information that can be used to construct effective numerical models of such phenomena.

The high-frequency air pressure and sea level oscillations have been quantified with a function fitted to the observations. Furthermore, the fact that the best fit for all three atmospheric disturbances was achieved using a bell-shaped function implies that this might be a common cross-propagation structure for mesoscale atmospheric disturbances that can be applied to future models. The narrowness of the most intense zones of the atmospheric disturbances partly explains why meteotsunamis

commonly impact only a limited segment of the coast (cf. Heidarzadeh et al. 2020; Candella and de Araujo 2021). Another crucial factor explaining the selective response of the sea level to passing pressure disturbances is the resonant nature of meteotsunamis. More specifically, frequent pronounced meteotsunamis commonly occur only within identifiable "hot spots" (that is, in bays, inlets, and harbors with high Q-factors and strong amplification/resonant properties; Rabinovich 2009, 2020) and under "Proudman resonance" conditions when and where the speed of incoming atmospheric disturbances crossing the shelf resonantly match the speed of long oceanic waves (Monserrat et al. 2006; Šepić et al. 2015).

Extreme sea level oscillations with periods shorter than a couple of hours, such as infragravity waves and seiches/meteotsunamis, and those with longer periods, such as storm surges, have traditionally been examined separately (e.g., Danard et al. 2003; Thomson et al. 2009; Pugh and Woodworth 2014). Recently, however, comprehensive studies of the cumulative effect of various types of oscillations on the total coastal flood height have started to emerge (e.g., Heidarzadeh and Rabinovich 2021; Medvedev et al. 2022). These studies show that the contribution of various sea level oscillations is highly site dependent: at one location most of the observed height is from storm surge, while at another from a combination of surge and meteotsunami, and at a third from IG waves (or from some other combination). The vast set of data that we collected to study the events described herein allowed for an unprecedentedly detailed assessment of the temporal and spatial distributions of mesoscale atmospheric processes and sea level oscillations, both coastal and offshore. Our results confirm that the sea level response is highly spatially dependent. In addition, we have identified the reasons for the spatial variability, which include both coastal topography and bathymetry and highly changeable atmospheric forcing. Access to atmospheric data from the dense VS network (and from CHS, NOAA, and ASOS stations) enabled us to precisely estimate a variety of properties, such as MSLP depth, rate of MSLP change, and associated winds. The propagation parameters of the three lows (L1, L2, and L3) and of the three strong air pressure disturbances (AD1, AD2, and AD3) that passed over the area allowed us, for the first time, to estimate cross-propagation parameters of the air pressure disturbances—and to show that they are best approximated by a relatively steep bell-shaped function.

In summary, our findings demonstrate the need for high-precision meteorological measurements both for understanding the underlying dynamics of extreme sea level events and for developing real-time forecasting models of their occurrences. Although there have been a few studies that have used numerical models to examine the generation of extreme sea level response by intense meteorological forcing, these models often fail to adequately reproduce the spatial and temporal variability of the sea level heights (cf. Renault et al. 2011). In contrast, we have used a high-resolution ocean model forced by well-resolved air pressure observations that enabled us to reproduce the recorded meteotsunami with very high precision.

REFERENCES

Aida, I., D. Date, and M. Koyama, 1970: On the characteristics of long-period fluctuations of the water level observed at Miyagi-Enoshima (in Japanese with English abstract and figure captions). *Bull. Earth Res.*, **48**, 983–997.

Candella, R. N., and C. E. S. de Araujo, 2021: Meteotsunamis in Brazil: An overview of known occurrences from 1977 to 2020. *Nat. Hazards*, **106**, 1563–1579, https://doi.org/10.1007/s11069-020-04331-y.

Danard, M., A. Munro, and T. Murty, 2003: Storm surge hazard in Canada. *Nat. Hazards*, **28**, 407–434, https://doi.org/10.1023/A:1022990310410.

Dzvonkovskaya, A., 2018: HF surface wave radar for tsunami alerting: From system concept and simulations to integration into early warning systems. *IEEE Aerosp. Electron. Syst. Mag.*, **33**, 48–58, https://doi.org/10.1109/MAES.2018.160267.

Eckart, C., 1951: Surface waves in water of variable depth. Scripps Institution of Oceanography Wave Rep. 100, S10, Ref. 51-12, 99 pp.

Fine, I. V., J. Y. Cherniawsky, R. E. Thomson, A. B. Rabinovich, and M. V. Krassovski, 2015: Observations and numerical modeling of the 2012 Haida Gwaii tsunami off the coast of

British Columbia. *Pure Appl. Geophys.*, **172**, 699–718, https://doi.org/10.1007/s00024-014-1012-7.

Gerritsen, F., and J. Van Heteren, 1984: Low frequency oscillations on the Dutch coast. *Proc. 19th Coastal Engineering Conf.*, Houston, TX, ASCE, 625–641.

Heidarzadeh, M., and A. B. Rabinovich, 2021: Combined hazard of typhoon-generated meteorological tsunamis and storm surges along the coast of Japan. *Nat. Hazards*, **106**, 1639–1672, https://doi.org/10.1007/s11069-020-04448-0.

——, J. Šepić, A. Rabinovich, M. Allahyar, A. Soltanpour, and F. Tavakoli, 2020: Meteorological tsunami of 19 March 2017 in the Persian Gulf: Observations and analyses. *Pure Appl. Geophys.*, **177**, 1231–1259, https://doi.org/10.1007/s00024-019-02263-8.

Hersbach, H., and Coauthors, 2020: The ERA5 global reanalysis. *Quart. J. Roy. Meteor. Soc.*, **146**, 1999–2049, https://doi.org/10.1002/qj.3803.

Huntley, D. A., and C. S. Kim, 1984: Is surf beat forced or free? *Proc. 19th Coastal Engineering Conf.*, Houston, TX, ASCE, 871–885.

Kovalev, P. D., A. B. Rabinovich, and G. V. Shevchenko, 1991: Investigation of long waves in the tsunami frequency band on the southwestern shelf of Kamchatka. *Nat. Hazards*, **4**, 141–159, https://doi.org/10.1007/BF00162784.

Lamb, H., 1945: *Hydrodynamics.* 6th ed. Dover, 760 pp.

LeBlond, P. H., and L. A. Mysak, 1978: *Waves in the Ocean.* Elsevier, 602 pp.

Medvedev, I. P., A. B. Rabinovich, and J. Šepić, 2022: Destructive coastal sea level oscillations generated by Typhoon Maysak in the Sea of Japan in September 2020. *Sci. Rep.*, **12**, 8463, https://doi.org/10.1038/s41598-022-12189-2.

Mercer, D., J. Sheng, R. J. Greatbatch, and J. Bobanović, 2002: Barotropic waves generated by storms moving rapidly over shallow water. *J. Geophys. Res.*, **107**, 3152, https://doi.org/10.1029/2001JC001140.

Monserrat, S., I. Vilibić, and A. B. Rabinovich, 2006: Meteotsunamis: Atmospherically induced destructive ocean waves in the tsunami frequency band. *Nat. Hazards Earth Syst. Sci.*, **6**, 1035–1051, https://doi.org/10.5194/nhess-6-1035-2006.

Pugh, D., and P. Woodworth, 2014: *Sea-Level Science: Understanding Tides, Surges, Tsunamis and Mean Sea-Level Changes.* Cambridge University Press, 395 pp.

Rabinovich, A. B., 2009: Seiches and harbor oscillations. *Handbook of Coastal and Ocean Engineering*, Y. C. Kim, Ed., World Scientific, 193–236.

——, 2020: Twenty-seven years of progress in the science of meteorological tsunamis following the 1992 Daytona Beach event. *Pure Appl. Geophys.*, **177**, 1193–1230, https://doi.org/10.1007/s00024-019-02349-3.

——, and F. E. Stephenson, 2004: Longwave measurements for the coast of British Columbia and improvements to the tsunami warning capability. *Nat. Hazards*, **32**, 313–343, https://doi.org/10.1023/B:NHAZ.0000035549.26392.c8.

——, and M. C. Eblé, 2015: Deep ocean measurements of tsunami waves. *Pure Appl. Geophys.*, **172**, 3281–3312, https://doi.org/10.1007/s00024-015-1058-1.

——, R. E. Thomson, and I. V. Fine, 2013: The 2010 Chilean tsunami off the west coast of Canada and the northwest coast of the United States. *Pure Appl. Geophys.*, **170**, 1529–1565, https://doi.org/10.1007/s00024-012-0541-1.

——, ——, M. V. Krassovski, F. E. Stephenson, and D. C. Sinnott, 2019: Five great tsunamis of the 20th century as recorded on

the coast of British Columbia. *Pure Appl. Geophys.*, **176**, 2887–2924, https://doi.org/10.1007/s00024-019-02133-3.

——, J. Šepić, and R. E. Thomson, 2021: The meteorological tsunami of 1 November 2010 in the southern Strait of Georgia: A case study. *Nat. Hazards*, **106**, 1503–1544, https://doi.org/10.1007/s11069-020-04203-5.

Renault, L., G. Vizoso, A. Jansá, J. Wilkin, and J. Tintoré, 2011: Toward the predictability of meteotsunamis in the Balearic Sea using regional nested atmosphere and ocean models. *Geophys. Res. Lett.*, **38**, L10601, https://doi.org/10.1029/2011GL047361.

Šepić, J., and A. B. Rabinovich, 2014: Meteotsunamis in the Great Lakes and on the Atlantic coast of the United States generated by the "derecho" of 29–30 June 2012. *Nat. Hazards*, **74**, 75–107, https://doi.org/10.1007/s11069-014-1310-5.

——, I. Vilibić, and I. Fine, 2015: Northern Adriatic meteorological tsunamis: Assessment of their potential through ocean modelling experiments. *J. Geophys. Res. Oceans*, **120**, 2993–3010, https://doi.org/10.1002/2015JC010795.

——, A. B. Rabinovich, and V. N. Sytov, 2018: Odessa tsunami of 27 June 2014: Observations and numerical modelling. *Pure Appl. Geophys.*, **175**, 1545–1572, https://doi.org/10.1007/s00024-017-1729-1.

Thomson, R. E., and W. J. Emery, 2014: *Data Analysis Methods in Physical Oceanography*. 3rd ed. Elsevier Science, 728 pp.

——, and I. V. Fine, 2021: Revisiting the ocean's non-isostatic response to 5-day atmospheric loading: New results based on global bottom pressure records and numerical modeling. *J. Phys. Oceanogr.*, **51**, 2845–2859, https://doi.org/10.1175/JPO-D-21-0025.1.

——, A. B. Rabinovich, and M. V. Krassovski, 2007: Double jeopardy: Concurrent arrival of the 2004 Sumatra tsunami and storm-generated waves on the Atlantic coast of the United States and Canada. *Geophys. Res. Lett.*, **34**, L15607, https://doi.org/10.1029/2007GL030685.

——, ——, I. V. Fine, D. C. Sinnott, A. McCarthy, N. A. S. Sutherland, and L. K. Neil, 2009: Meteorological tsunamis on the coasts of the British Columbia and Washington. *Phys. Chem. Earth*, **34**, 971–988, https://doi.org/10.1016/j.pce.2009.10.003.

——, I. V. Fine, A. B. Rabinovich, S. Mihály, E. E. Davis, M. Heesemann, and M. V. Krassovski, 2011: Observation of the 2009 Samoa tsunami by the NEPTUNE-Canada cabled observatory: Test data for an operational regional tsunami forecast model. *Geophys. Res. Lett.*, **38**, L11701, https://doi.org/10.1029/2011GL046728.

Titov, V., and C. Moore, 2021: Meteotsunami model forecast: Can coastal hazard be quantified in real time? *Nat. Hazards*, **106**, 1545–1561, https://doi.org/10.1007/s11069-020-04450-6.

Vennell, R., 2007: Long barotropic waves generated by a storm crossing topography. *J. Phys. Oceanogr.*, **37**, 2809–2823, https://doi.org/10.1175/2007JPO3687.1.

Wang, K., R. E. Thomson, A. B. Rabinovich, I. V. Fine, and T. L. Insua, 2020: The 2018 Alaska-Kodiak tsunami off the west coast of North America: A rare mid plate tsunamigenic event. *Pure Appl. Geophys.*, **177**, 1347–1378, https://doi.org/10.1007/s00024-020-02427-x.

Weaver, A. J., and E. C. Wiebe, 2006: Micro Meteorological Network in Greater Victoria Schools—www.victoriaweather.ca. University of Victoria School of Earth and Ocean Sciences Bulletin, 10 pp., https://www.islandweather.ca/resources/info/2006CMOSBulletin.pdf.

Webb, S. C., X. Zhang, and W. Crawford, 1991: Infragravity waves in the deep ocean. *J. Geophys. Res.*, **96**, 2723–2736, https://doi.org/10.1029/90JC02212.

Williams, D. A., K. J. Horsburgh, D. M. Schultz, and C. W. Hughes, 2019: Examination of generation mechanisms for an English Channel meteotsunami: Combining observations and modeling. *J. Phys. Oceanogr.*, **49**, 103–120, https://doi.org/10.1175/JPO-D-18-0161.1.